

# Phase Angle Dependent Ultraviolet to Far-Infrared (0.25-100 $\mu\text{m}$ ) Reflectance Spectroscopy of Mukundpura (CM2) Meteorite: Potential analogue of (162173) Ryugu and (101955) Bennu

Varatharajan Indhu<sup>1</sup>, Maturilli Alessandro<sup>2</sup>, Sivaraman Bhala<sup>3</sup>, Helbert Jorn<sup>2</sup>, Grott Matthias<sup>4</sup>, Meka J. K.<sup>3</sup>, Vijayan S<sup>3</sup>, and Bhardwaj Anil<sup>3</sup>

<sup>1</sup>German Aerospace Center (DLR)

<sup>2</sup>DLR

<sup>3</sup>Physical Research Laboratory

<sup>4</sup>DLR Institute for Planetary Research

November 16, 2022

## Abstract

Specialized spectral library measured under controlled planetary surface conditions is important to accurately derive the chemical and physical properties from remote observations. It's a general practice to powder the planetary analogues during spectroscopy studies as most surfaces are made up of fine-regolith materials. However, upon arrival at C-type asteroids Ryugu and Bennu, Hayabusa2 and OSIRIS-REx revealed these surfaces filled with rocks and boulders. In this study, we built a phase angle dependent ultraviolet (UV) to far-infrared (FIR) spectroscopy (0.2-100  $\mu\text{m}$ ) of a rocky piece of Mukundpura meteorite having five surfaces including fusion crust. Mukundpura meteorite is the freshest carbonaceous chondrite belonging to CM-chondrites in the entire collection which fell in the desert village of India on June 6, 2017. The two sets of varying viewing geometries having incident and reflectance angles includes ; a) asymmetric viewing geometry at 13°-13°, 13°-20°, 13°-30°, 13°-40°, and 13°-50°, and b) symmetric viewing geometry at 13°-13°, 20°-20°, 30°-30°, 40°-40°, and 50°-50°. This study found that overall spectral shape, reflectance values, and band depth of diagnostic absorption features are affected by viewing geometry and surface roughness; however, the fundamental band centers are not affected. The comparison of 2.72  $\mu\text{m}$  absorption band of fusion crust and fresh interiors of Mukundpura with published Ryugu and Bennu spectra supports that Ryugu surface has experienced extensive heating in its geologic past compared to Bennu. Overall study shows that fusion crust and internal surfaces of the Mukundpura meteorite is a potential analogue of Ryugu and Bennu both spectrally and morphologically.

## Hosted file

supporting information\_agu.docx available at <https://authorea.com/users/523491/articles/595246-phase-angle-dependent-ultraviolet-to-far-infrared-0-25-100-%CE%BCm-reflectance-spectroscopy-of-mukundpura-cm2-meteorite-potential-analogue-of-162173-ryugu-and-101955-bennu>

1           **Phase Angle Dependent Ultraviolet to Far-Infrared (0.25-100  $\mu\text{m}$ ) Reflectance**  
2           **Spectroscopy of Mukundpura (CM2) Meteorite: Potential analogue of (162173)**  
3           **Ryugu and (101955) Bennu**

4  
5           **I. Varatharajan<sup>1\*</sup>, A. Maturilli<sup>1</sup>, B. Sivaraman<sup>2</sup>, J. Helbert<sup>1</sup>, M. Grott<sup>1</sup>, J.K. Meka<sup>2</sup>, S.**  
6           **Vijayan<sup>2</sup>, and A. Bhardwaj<sup>2</sup>**

7           <sup>1</sup>Institute for Planetary Research, German Aerospace Center DLR, Rutherfordstraße 2, 12489  
8           Berlin, Germany.

9           <sup>2</sup> Physical Research Laboratory, Navrangpura, Ahmedabad, Gujarat 380009, India.

10  
11           Corresponding author: Indhu Varatharajan ([indhu.varatharajan@dlr.de](mailto:indhu.varatharajan@dlr.de))

12  
13  
14           **Key Points:**

- 15           • Band depth of diagnostic absorption features change strongly but systematically with  
16           varying viewing geometry.
- 17           • Band center of diagnostic absorption features centers are not affected by varying viewing  
18           geometry.
- 19           • Nature of 2.72  $\mu\text{m}$  absorption band of Ryugu with Mukundpura fusion crust supports  
20           extensive heating in Ryugu's geologic past.  
21

## 22 Abstract

23 Specialized spectral library measured under controlled planetary surface conditions is important  
24 to accurately derive the chemical and physical properties from remote observations. It's a general  
25 practice to powder the planetary analogues during spectroscopy studies as most surfaces are  
26 made up of fine-regolith materials. However, upon arrival at C-type asteroids Ryugu and Bennu,  
27 Hayabusa2 and OSIRIS-REx revealed these surfaces filled with rocks and boulders. In this  
28 study, we built a phase angle dependent ultraviolet (UV) to far-infrared (FIR) spectroscopy (0.2-  
29 100  $\mu\text{m}$ ) of a rocky piece of Mukundpura meteorite having five surfaces including fusion crust.  
30 Mukundpura meteorite is the freshest carbonaceous chondrite belonging to CM-chondrites in the  
31 entire collection which fell in the desert village of India on June 6, 2017. The two sets of varying  
32 viewing geometries having incident and reflectance angles includes ; a) asymmetric viewing  
33 geometry at 13°-13°, 13°-20°, 13°-30°, 13°-40°, and 13°-50°, and b) symmetric viewing  
34 geometry at 13°-13°, 20°-20°, 30°-30°, 40°-40°, and 50°-50°. This study found that overall  
35 spectral shape, reflectance values, and band depth of diagnostic absorption features are affected  
36 by viewing geometry and surface roughness; however, the fundamental band centers are not  
37 affected. The comparison of 2.72  $\mu\text{m}$  absorption band of fusion crust and fresh interiors of  
38 Mukundpura with published Ryugu and Bennu spectra supports that Ryugu surface has  
39 experienced extensive heating in its geologic past compared to Bennu. Overall study shows that  
40 fusion crust and internal surfaces of the Mukundpura meteorite is a potential analogue of Ryugu  
41 and Bennu both spectrally and morphologically.

42 Keywords: Mukundpura, spectroscopy, C-type asteroids, phase angle, meteorite

43

## 44 Plain Language Summary

45 JAXA's Hayabusa2 and NASA's OSIRIS-REx are currently exploring two carbon-rich near-  
46 earth asteroids namely Ryugu and Bennu respectively. Different minerals characteristically  
47 absorb the received sun's energy at different wavelengths of sun's electromagnetic spectrum.  
48 Therefore, spectra recorded at wide spectral range are used as finger-prints to find the nature of  
49 minerals remote observations. However, one of the parameters that affects the spectra is viewing  
50 geometry between sun-surface-satellite. The spectrometers onboard these missions found that  
51 both asteroids possess rocky surface instead of fine-powdered soils. In this study, we spectrally  
52 investigated the non-powdered fresh carbonaceous meteorite named Mukundpura which fell in  
53 India on June, 2017 for varying viewing geometries. The sample studied has five surfaces  
54 including fusion crust. This study found that overall shape and absorption strength at  
55 characteristic wavelengths of spectra is affected by varying viewing geometry and surface  
56 roughness, however, the finger-print energy of absorption defined as band centers are not  
57 affected by these effects. The results from fusion crust and fresh meteorite surface are further  
58 compared with Ryugu and Bennu support that Ryugu surface had experienced extensive heating  
59 compared to Bennu. Overall our study shows that studied Mukundpura meteorite is a potential  
60 equivalent of Ryugu and Bennu both chemically and physically.

61

## 62 1 Introduction

63 Carbonaceous chondrites (CC) form the most important group of primitive extraterrestrial  
64 rocks that have recorded the earliest processes in the origin and evolution of solar system that  
65 includes formation of chondrules and refractory inclusions, heating records of short-lived

66 radionuclides, formation of planetesimals/asteroids by accretion, thermal evolution, and aqueous  
67 alteration of minerals within them [Anders and Grevesse, 1989]. Although CCs occupy a major  
68 fraction (75%) among asteroids, CCs only account for 4.4% including falls and finds in Earth's  
69 meteorite inventory [Barrat *et al.*, 2012]. This limits us in understanding the diversity in  
70 mineralogy and composition of C-type asteroids.

71 On June 6, 2017, a meteorite weighing ~2 kg fell in Mukundpura village (26° 52' 53"N,  
72 75° 39' 54"E) of Rajasthan, India. This impact formed a nearly circular crater of ~43 cm in  
73 diameter with a depth of ~15 cm and the impactor shattered into several large pieces and  
74 numerous small pieces which weigh from gram to subgram-sized fragments [GSI, 2017; Ray and  
75 Shukla, 2018]. Mukundpura meteorite fragments were collected immediately after the reported  
76 fall and the main mass was secured by Geological Survey of India (GSI), Kolkata repository.  
77 The collected inner part of the meteorite was dark and fine to very fine grained with the  
78 development of ~1.5-2 mm thick "glossy" fusion crust containing oxidized metal and sulfides  
79 within the silicate matrix. [GSI, 2017] also noticed a "very strong sulfur smell" with the samples.

80 Ray and Shukla [2018] and Rudraswami *et al.* [2018] studied the petrography,  
81 mineralogy, isotopes, and bulk chemical composition of the samples collected and classified it as  
82 a CM2 class of carbonaceous chondrites. Therefore, Mukundpura meteorite is an extremely fresh  
83 carbonaceous chondrite in the entire CC collection. The cathode-luminescence study of the  
84 meteorite reveals [Baliyan and Ray, 2019] various clast and matrix-rich made of varieties of  
85 phyllosilicates, Mg-serpentine, Fe-cronstedtite, tochilinite along with; a) few relict chondrules  
86 made of highly forsteritic porphyritic olivine, barred olivine, and porphyritic pyroxene, b)  
87 isolated, subhedral olivine grains - both forsteritic ( $\text{Fo}_{98.74-99.66}$ ) and fayalitic ( $\text{Fa}_{50}$ ), c) poorly  
88 characterized phases of phyllosilicates, d) other minor and accessory phases, which includes  
89 carbonates and sulfides and e) the olivine grains within the Mukundpura meteorite suggests  
90 intense and multiple phases of complex aqueous alteration in the parent body. Potin *et al.* [2018]  
91 analysis of Mukundpura using Raman spectroscopy further confirms that Mukundpura meteorite  
92 is a primitive CM2 chondrite having escaped any significant heating including radiogenic and  
93 shock-related metamorphism.

94 Two sample return missions to C-type Near Earth Asteroids (NEAs), JAXA's Hayabusa2  
95 mission to (162173) Ryugu (1999 JU3) and NASA's Origins, Spectral Investigation, Resource  
96 Identification, Security-Regolith Explorer (OSIRIS-REx) mission to (101955) Bennu, carry  
97 spectrometers of varying spectral ranges for remote sensing mapping.

98 Hayabusa2 carries two onboard remote sensing spectrometers; The Telescopic Optical  
99 Navigation Camera (ONC-T) with seven color filters (ul: 0.40  $\mu\text{m}$ , b: 0.48  $\mu\text{m}$ , v: 0.55  $\mu\text{m}$ , Na:  
100 0.59  $\mu\text{m}$ , w: 0.70  $\mu\text{m}$ , x: 0.86  $\mu\text{m}$ , and p: 0.95  $\mu\text{m}$ ) [Tatsumi *et al.*, 2019] and the Near-Infrared  
101 Spectrometer (NIRS3) operating in scanning mode and collecting reflectance spectra in the range  
102 from 1.8 – 3.2  $\mu\text{m}$  with spectral sampling resolution of 18 nm.

103 OSIRIS-REx carries two spectrometers; OSIRIS-REx Visible and Infrared Spectrometer  
104 (OVIRS) which covers the spectral range of 0.4–4.3  $\mu\text{m}$  with a 4-mrad field of view (FOV) and a  
105 spectral sampling of 2 nm from 0.392 to 2.4  $\mu\text{m}$ , and 5 nm from 2.4 to 4.3  $\mu\text{m}$  [Reuter *et al.*,  
106 2018; Simon *et al.*, 2018], and OSIRIS-REx Thermal Emission Spectrometer (OTES), which  
107 covers the spectral range 5.5–100  $\mu\text{m}$  with an 8-mrad FOV and a spectral sampling of 8.66  $\text{cm}^{-1}$   
108 [Christensen *et al.*, 2018]; both aiming to map the spatially resolved global composition at 20 m  
109 and 40 m respectively.

110 Hayabusa2 and OSIRIS-REx shows that both Ryugu and Bennu are very dark top-shaped  
111 body (visible albedo of 4.6% with photometry standard reflectance lower than 2% [Sugita *et al.*,

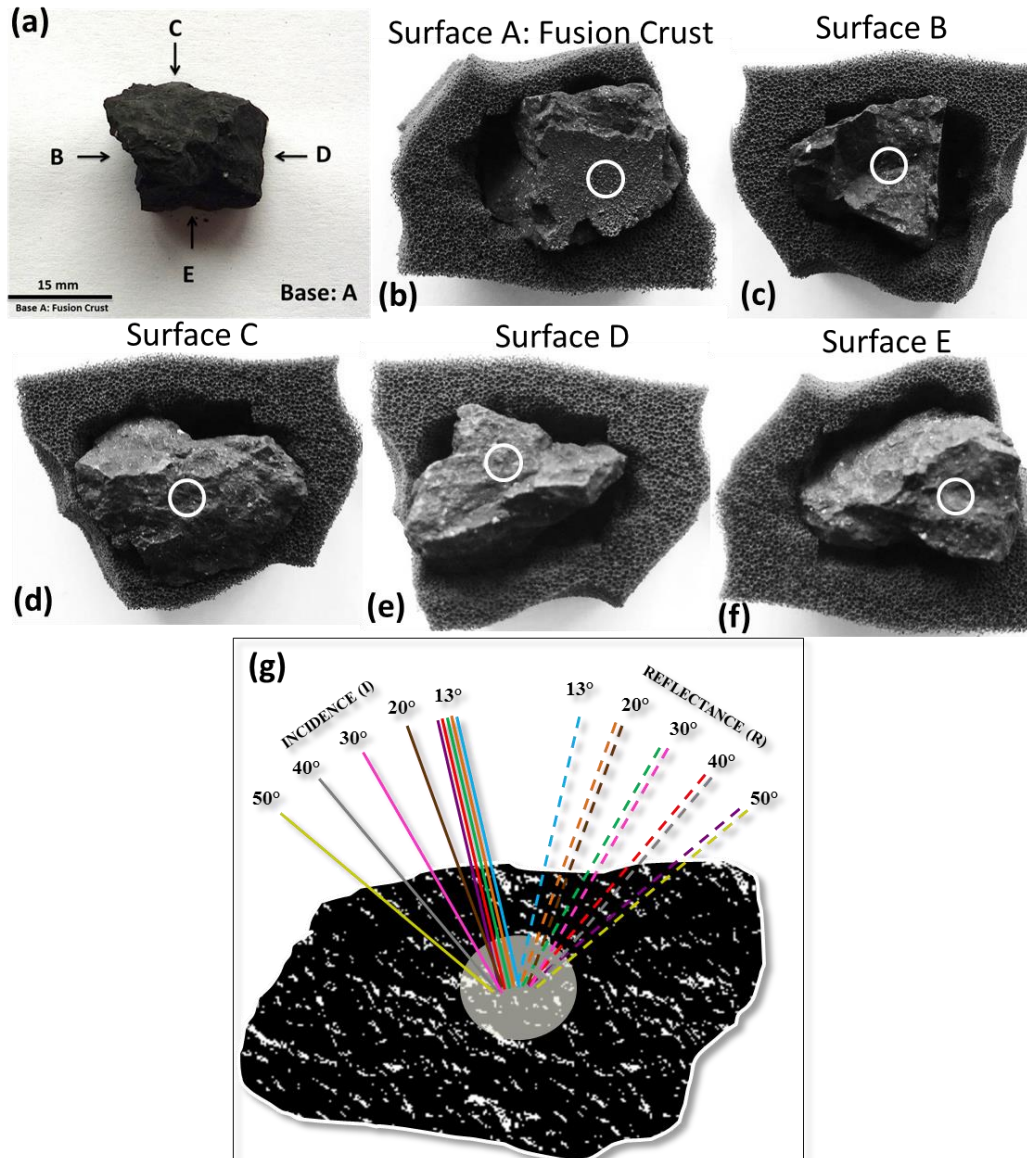
112 2019] for Ryugu) with a very rocky surface covered by numerous boulders (10 cm to 10 m sized  
113 boulders for Ryugu) with almost no regolith [*DellaGiustina et al.*, 2019; *Lauretta et al.*, 2019;  
114 *Sugita et al.*, 2019; *Walsh et al.*, 2019; *Watanabe et al.*, 2019]. For a correct interpretation of the  
115 remote sensing spectral data it is therefore important to understand the spectral behaviour of CCs  
116 having varying 3-dimensional (3D) surface roughness (not just powders) belonging to this  
117 particular asteroid class (C-type) at wide spectral range from ultraviolet (UV: 0.25  $\mu\text{m}$ ) to far-  
118 infrared (FIR: 100  $\mu\text{m}$ ) and varying phase angle combinations.

119 *Beck et al.* [2018], *Jacinto et al.* [2013], and *Malavergne et al.* [2014] studied the  
120 laboratory spectroscopy of various powdered carbonaceous chondrites of varying grain sizes  
121 under vacuum conditions to characterise their corresponding asteroid parent bodies. However,  
122 the dependency of the reflectance spectra on their varying observation geometry and phase  
123 angles for its corresponding spectral regions is still largely unknown for these chondrites [*Beck et*  
124 *al.*, 2018]. In a recent study, *Potin et al.* [2019] studied the varying spectral nature of the  
125 Mukundpura chip and powder corresponding to varying viewing geometries and temperatures  
126 but limiting to VNIR spectral region (0.34 - 5  $\mu\text{m}$ ) in order to characterise the NEAs and found  
127 that the spectral slopes, reflectance values, and absorption bands are affected by these effects.

128 In this study, we carried out reflectance spectroscopy of the fresh Mukundpura CM2  
129 meteorite rock (non-powdered) at wide spectral range (UV:0.2- FIR:100  $\mu\text{m}$ ) under varying  
130 viewing geometries with phase angles varies from  $26^\circ$  to  $100^\circ$  respectively (Fig. 1). In addition  
131 to understanding the mineralogy of the Mukundpura (CM chondrite) from a spectroscopy  
132 standpoint, we also investigated the overall spectral behaviour (UV-FIR) of Mukundpura  
133 meteorite for its overall spectral shape, slope, absorption band centres, and band strength as a  
134 function of viewing geometry and surface roughness. Therefore, this study will help to carefully  
135 interpret the remote sensing and landing site spectra of the rocky surfaces of Ryugu, Bennu, and  
136 future missions exploring NEAs.

137

138



139

140

141

142 **Figure 1.** a) the scale of Mukundpura meteorite studied sitting on its fusion crust, b-f) different  
 143 surfaces (surfaces B-E) of Mukundpura sample where the white circle represents the (approx)  
 144 area of region studied for spectral analyses. The brightness and contrast of the picture is  
 145 enhanced to clear representation of roughness of the surface – resembling asteroid Ryugu, g) the  
 146 symmetric ( $13^{\circ}$ - $13^{\circ}$ ,  $20^{\circ}$ - $20^{\circ}$ ,  $30^{\circ}$ - $30^{\circ}$ ,  $40^{\circ}$ - $40^{\circ}$ ,  $50^{\circ}$ - $50^{\circ}$ ) and asymmetric ( $13^{\circ}$ - $13^{\circ}$ ,  $13^{\circ}$ - $20^{\circ}$ ,  $13^{\circ}$ -  
 147  $30^{\circ}$ ,  $13^{\circ}$ - $40^{\circ}$ ,  $13^{\circ}$ - $50^{\circ}$ ) viewing geometries with varying phase angles considered in this study.

148

## 149 2 Sample

150 In this study we used a small sample from the fresh Mukundpura meteorite (CM  
 151 chondrite) (Fig. 1) without powdering it. This provides a better morphological analog since the  
 152 sample closely resembles the rocky surface of Ryugu and Bennu. The sample collected (Fig. 1a)

153 has five different surfaces/sides including the fusion crust (Fig. 1b; surface A) and four interior  
154 surfaces (Fig. 1c-f; surfaces B-E). During the impact parts of Mukundpura broke into small  
155 fragments and the sample collected and studied in this manuscript has a surface exhibiting fusion  
156 crust (surface A) and the fresh interior surfaces (surfaces B-E). By measuring the mass (5.7841  
157 gm) and computing the volume ( $2.5426 \text{ cm}^3$ ), we then calculated the bulk density  
158 ( $=\text{mass}/\text{volume}$ ) of the Mukundpura sample and found to be  $2.2749 \text{ g/cm}^3$  typical for CM  
159 chondrites [Flynn *et al.*, 2018]. The computation of volume of the sample is enabled by 3D  
160 mapping of the sample using NextEngine3D scanner and its corresponding 3D shape (.stl format)  
161 is provided as supporting information.

162 The bright spots on the surface of the rock in Fig.1a indicate the presence of CAIs. The  
163 fusion crust (Fig. 1b; surface A) is nearly flat and glossy surface, which is a very thin layer  
164 formed due to melting of the outer surface as the meteorite falls through the atmosphere. Fig. 1b-  
165 f shows the surfaces of the Mukundpura meteorite studied, which is placed on the sponge sample  
166 holder in-order to fix them steadily while taking the measurements. The white circle placed on  
167 each surface in Fig. 1b-f indicates the approximate area studied in the spectral analyses for the  
168 respective spectral region for varying viewing geometry. The brightness and contrast of Fig. 1b-f  
169 is enhanced to emphasize the differences in the 3D surface roughness/topography of each of the  
170 surfaces resembling the rocky/boulder-rich surface on the asteroids Ryugu and Bennu.

171

### 172 **3 Methods**

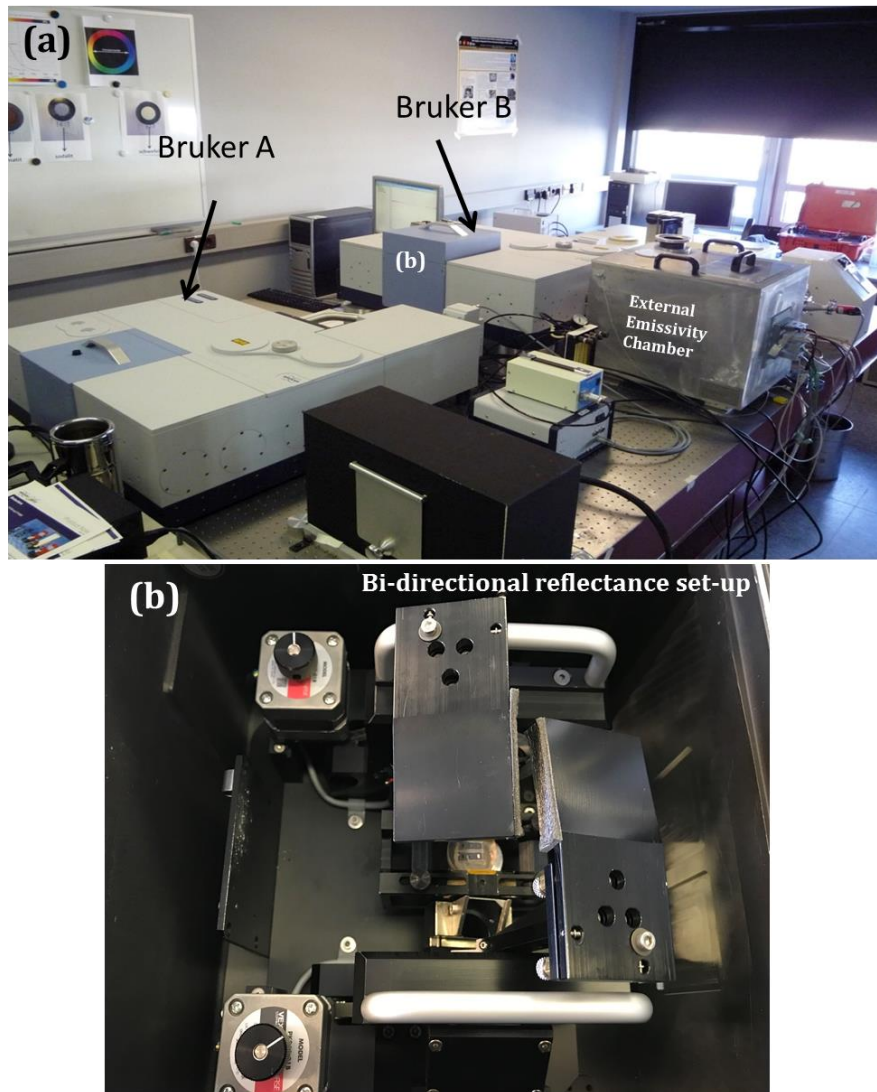
173 In this study, the phase angle dependent bi-conical reflectance spectroscopy of the  
174 Mukundpura sample is carried out at the Planetary Spectroscopy Laboratory (PSL) facility  
175 located at the Institute of Planetary Research (PF) at the German Aerospace Center (DLR),  
176 Berlin [Maturilli *et al.*, 2018b]. Two Bruker Vertex 80V instruments hosted at PSL are used for  
177 the reflectance measurements (Fig. 2a); one of the spectrometers (Bruker A; Fig. 2a) is equipped  
178 with aluminum mirrors and therefore optimized for spectral measurements in the ultraviolet (UV:  
179  $0.2\text{-}0.6 \mu\text{m}$ ), visible-infrared (VISIR:  $0.4\text{-}1 \mu\text{m}$ ) range, mid infrared (MIR:  $1\text{-}25 \mu\text{m}$ ), and the  
180 second one (Bruker B; Fig. 2) is equipped with gold-coated mirrors optimized for measurements  
181 in Far infrared (FIR:  $14\text{-}100 \mu\text{m}$ ).

182 Both the spectrometers (Bruker A and Bruker B) use a Bruker A513 variable-angle  
183 reflection accessory (Fig. 2b) attached with two mirrors enabling viewing cone with aperture of  
184  $17^\circ$  and therefore allowing bi-conical reflectance measurements under vacuum conditions for  
185 varying viewing geometry with phase angles between  $26^\circ$  and  $170^\circ$  [Beck *et al.*, 2018; Maturilli  
186 *et al.*, 2018a; Maturilli *et al.*, 2014].

187 The UV-FIR spectroscopy of each surface of the Mukundpura sample is conducted for  
188 two sets of varying viewing geometries for a total of nine phase angle combinations (Fig. 1g); a)  
189 asymmetric viewing geometry where incident angle is fixed near nadir ( $13^\circ$ ) and reflectance  
190 angles varied in steps:  $13^\circ\text{-}13^\circ$ ,  $13^\circ\text{-}20^\circ$ ,  $13^\circ\text{-}30^\circ$ ,  $13^\circ\text{-}40^\circ$ , and  $13^\circ\text{-}50^\circ$ , and b) symmetric  
191 viewing geometry, where both incidence and reflectance angles varied identically with respect  
192 to each other for each measurement which includes  $13^\circ\text{-}13^\circ$ ,  $20^\circ\text{-}20^\circ$ ,  $30^\circ\text{-}30^\circ$ ,  $40^\circ\text{-}40^\circ$ , and  $50^\circ\text{-}$   
193  $50^\circ$ . In order to achieve this, we obtained a total of 225 spectra (5 surfaces times 9 phase angle  
194 combinations times 5 sets of detector-beamsplitter configurations to cover the entire spectral  
195 range).

196 We collected bi-conical reflectance spectra under vacuum for five meteorite surfaces (A-  
197 E; Fig. 2) in the whole spectral range ( $\sim 0.2\text{-}100 \mu\text{m}$ ) using both spectrometers. The details of the  
198 beam-splitter and detector used for each spectral subset are tabulated in Table S1 in supporting

199 information. The reflectance of each Mukundpura surface was measured at a spectral resolution  
200 of  $\sim 4\text{cm}^{-1}$  using a spot size of 4 mm at nine different phase angle combinations. The references  
201 used for calibration in each spectral range are also listed in Table S1. The measured reflectance  
202 spectrum of each surface at each phase angle is then divided by the corresponding reflectance  
203 spectrum of the reference at the respective phase angle. For details on the step-by-step procedure  
204 of the reflectance measurements, see Text S1 of the supporting information. The average surface  
205 spectra (throughout the manuscript) is calculated by taking the mean of the spectra at their  
206 respective viewing geometry for the surfaces B, C, D, and E.  
207



208  
209  
210

211 **Figure 2.** a) Laboratory set-up at PSL. Both Bruker A and Bruker B are Bruker Vertex 80V  
212 FTIR spectrometers. Bruker A is optimized for measurements in UV, VIS-IR, TIR spectral range  
213 and Bruker B is optimized for measurements in FIR spectral range. Bruker B is also attached to  
214 an external emissivity chamber for direct emissivity measurements at very high temperatures. b)  
215 shows the bi-conical reflectance setup at PSL.

216

217

### 218 **3.1 Derivation of spectral parameters**

#### 219 **3.1.1 Continuum-Removal**

220 We have derived commonly used spectral parameters, such as band center and the band  
221 depth of diagnostic absorption features, to understand their behaviour with changing phase angle  
222 combinations and local surface roughness (e.g., Section 4.3). In order to achieve this, the  
223 reflectance spectra are first normalized with respect to a common baseline by adopting the  
224 continuum removal methodology by *Clark et al.* [1987] and *Clark and Roush* [1984]. This is  
225 achieved by first fitting the convex-hull over the absorption feature by anchoring the continuum  
226 shoulder points having maximum reflectance values on either side of the absorption feature.  
227 Continuum removed spectra are then derived by dividing the reflectance spectra with this  
228 continuum baseline.

229

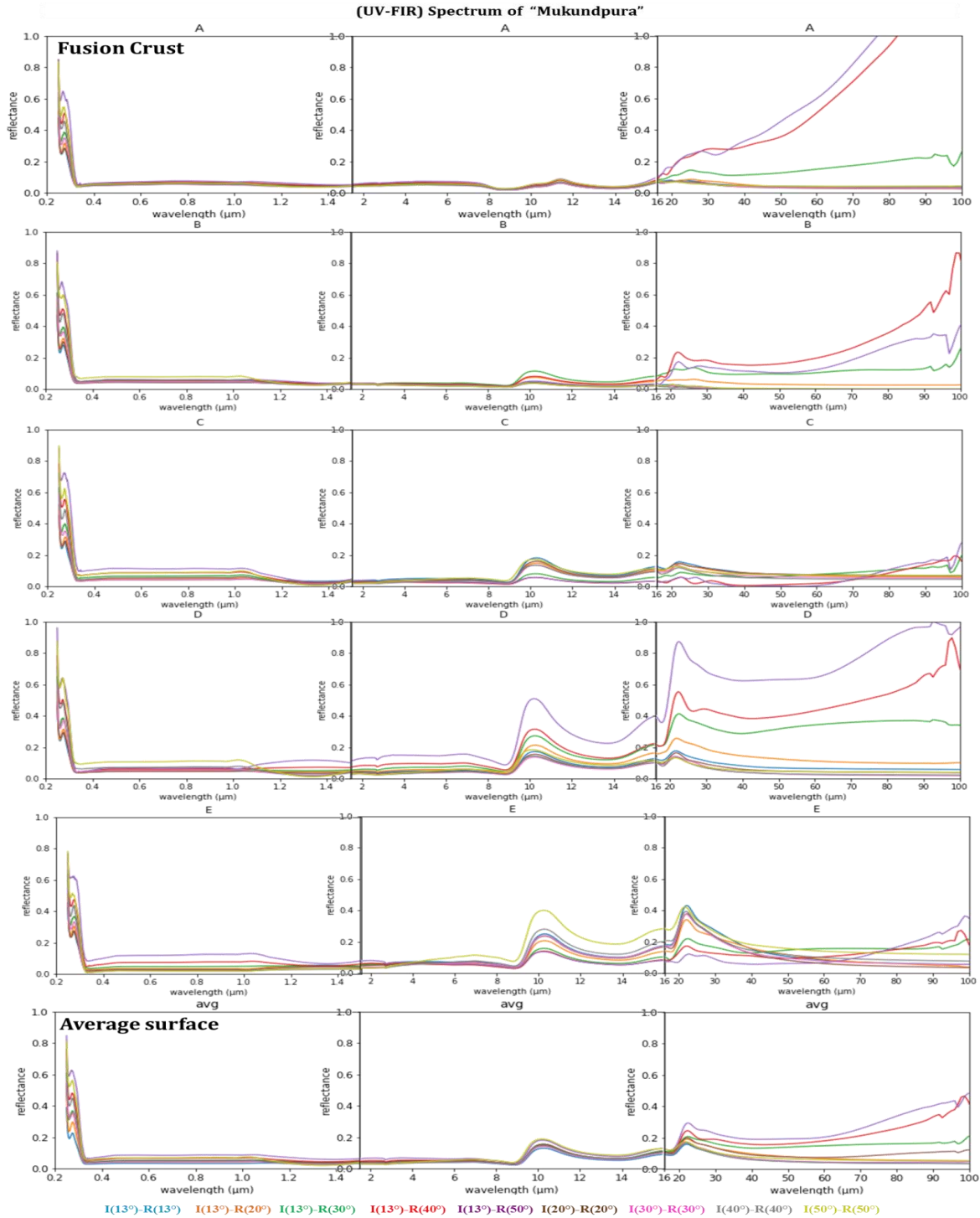
#### 230 **3.1.2 Band Center and Band Depth**

231 The band center is the wavelength of the band minima of a diagnostic absorption feature  
232 (where maximum absorption occurs) in the continuum removed spectra. Band depth is estimated  
233 as 1-continuum removed reflectance value at the calculated band minima i.e., band center.

234

### 235 **4 Results**

236 The UV-FIR spectra of Mukundpura sample for two sets of viewing geometries are  
237 shown in Fig. 3. The spectra of at phase angle combinations 13°-30° (green), 13°-40° (red), and  
238 13°-50° (violet), behaves relatively different with enhanced spectral features at longer  
239 wavelengths ( $> 9 \mu\text{m}$ ) irrespective of the surfaces compared to other viewing angles.



240

241

242 **Figure 3.** Measured UV-FIR spectra of fusion crust (A), intrinsic surfaces (B-E), and the average  
 243 spectra of surfaces (B-E) for its varying viewing geometry

244

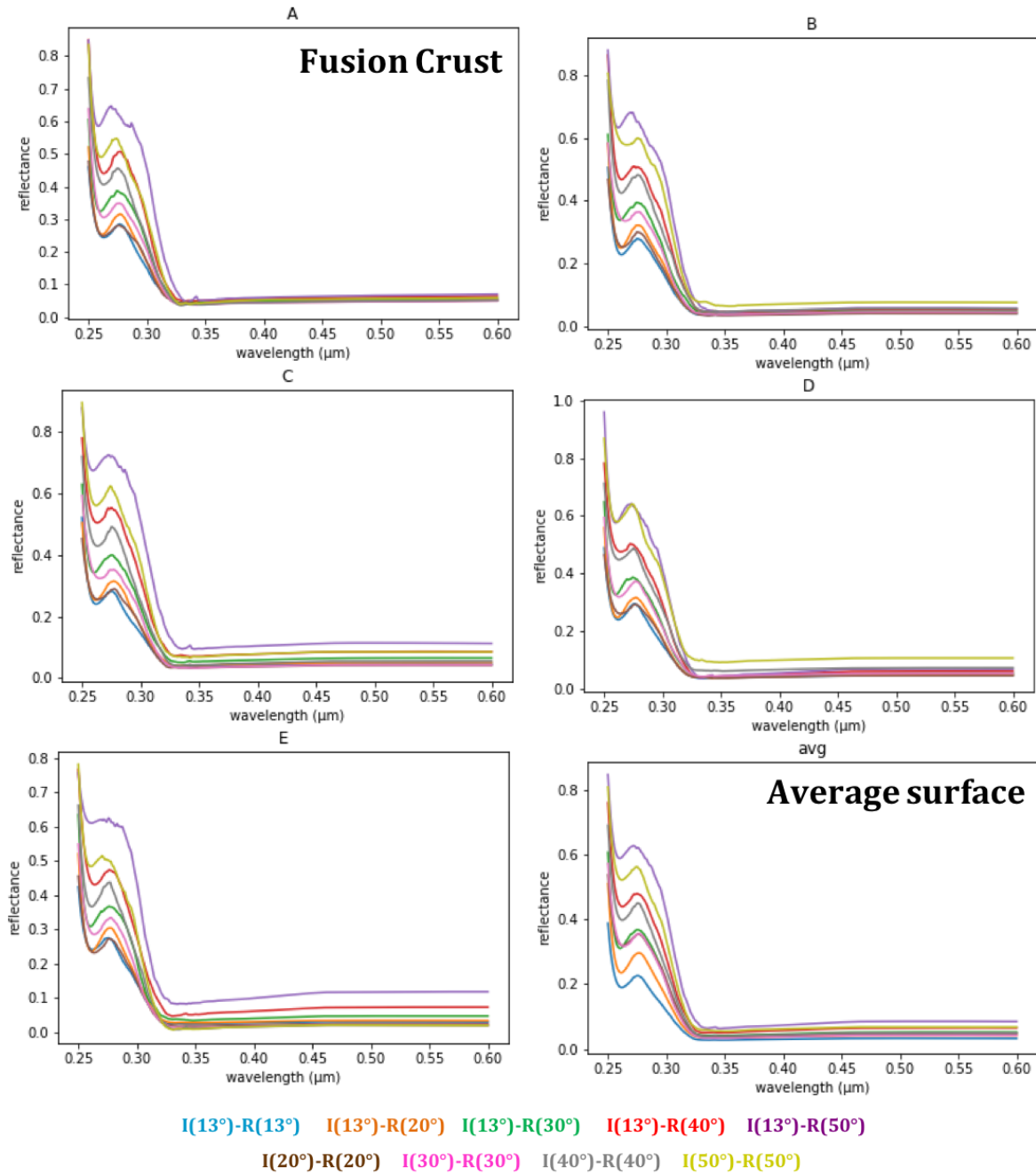
#### 245 **4.1 Ultraviolet (UV): 0.2-0.6 μm**

246 In the UV-VIS region, both fusion crust (Fig. 4A) and the other meteorite surfaces (Fig.  
 247 4B-E) show spectral characteristics; with strongest reflectance near 0.25 μm, a narrow

248 absorption feature near  $\sim 0.26 \mu\text{m}$  with reflectance peak at  $0.275 \mu\text{m}$ , a steeper bluer (negative)  
249 slope from  $0.27$  to  $0.325 \mu\text{m}$ , and a very low reflectance with nearly flat spectra from  $0.325$  to  
250  $0.6 \mu\text{m}$ . *Applin et al.* [2018] analysis on the UV reflectance spectra of carbonaceous materials  
251 reveals that all varieties of pure carbon revealed a Fresnel peak ( $\text{sp}^2 \pi-\pi^*$ ) short-ward of  $0.3 \mu\text{m}$   
252 and the position of this peak maximum changes with grain size and metamorphism and spectral  
253 contrast of Fresnel peak decreases with grain size where smaller grain sizes peaks near  $0.272 \mu\text{m}$   
254 and the larger macroscopic grained powders of amorphous carbon peaks near  $0.25 - 0.26 \mu\text{m}$ .  
255 Therefore, the Fresnel peaks near  $0.25 \mu\text{m}$  and  $0.275 \mu\text{m}$  of fusion crust and surface spectra of  
256 Mukundpura suggests the presence of nanophase graphite or amorphous carbon in the matrix  
257 [*Applin et al.*, 2018].

258 For all the five sides of the meteorite (Fig. 4 A-E), the reflectance value at Fresnel peak  
259 near  $0.275 \mu\text{m}$  and thereby the spectral slope between  $0.275-0.325 \mu\text{m}$  increases with increasing  
260 reflectance angle irrespective of their incidence angle. For all the five surfaces, longward of  
261  $0.325 \mu\text{m}$  the spectral variation diminishes, and no distinguishable signature is present at any  
262 viewing geometry. This suggests that, irrespective of the surface roughness, the UV-VIS spectral  
263 nature of Mukundpura sample have similar behavior at their respective phase angle observations.  
264 Altogether, it corresponds to the presence of carbon rich matrix within all surfaces including  
265 fusion crust [*Applin et al.*, 2018]. The dark carbonaceous material in visible region is highly  
266 reflective in the UV region ( $0.25-0.3 \mu\text{m}$ ).

### (UV-VIS) Spectrum of Mukundpura



267  
268  
269  
270

**Figure 4.** UV spectra of fusion crust (A), intrinsic surfaces (B-E), and the average spectra of surfaces (B-E) for its varying viewing geometry

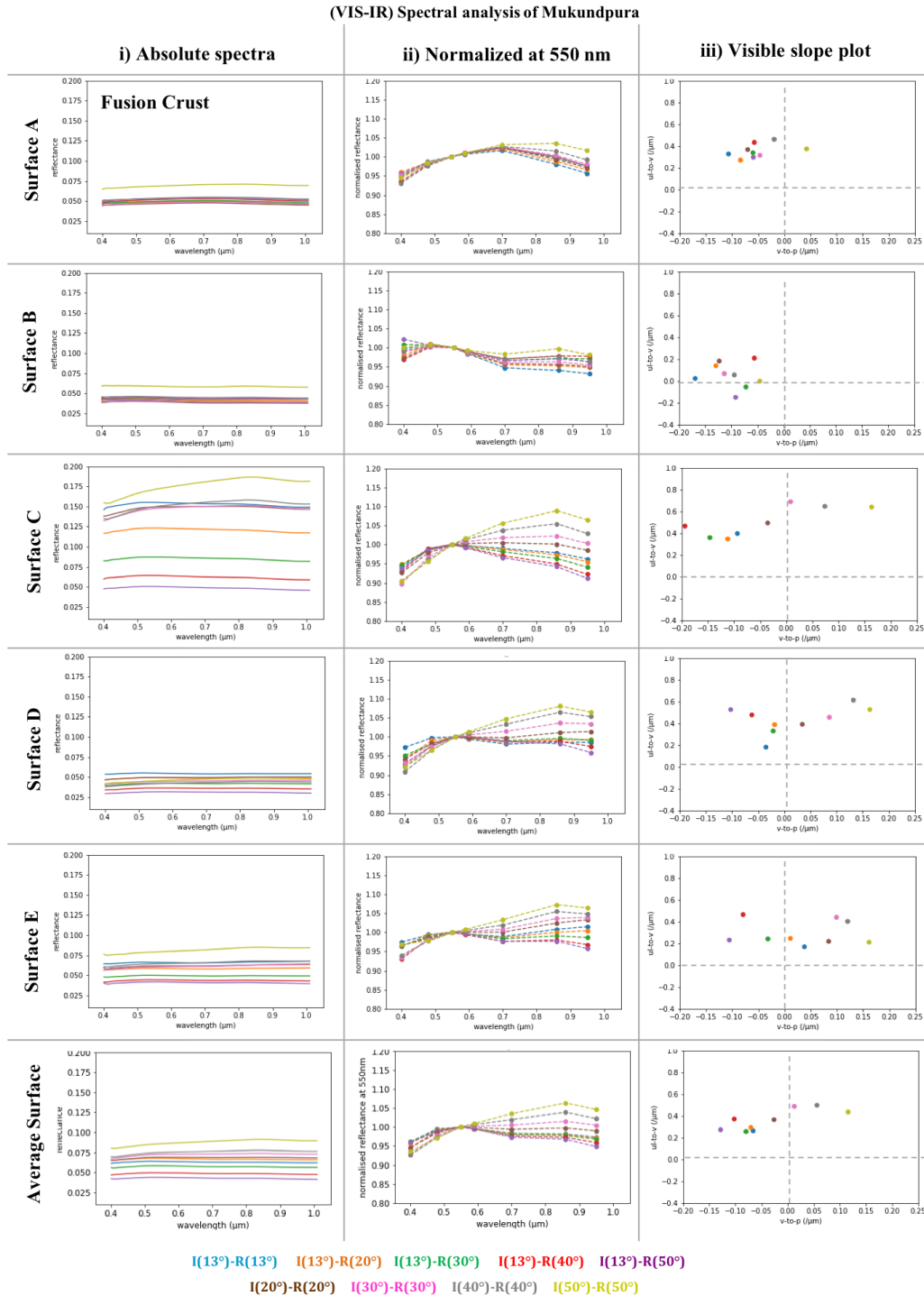
#### 4.2 Visible – Infrared (VIS-IR): 0.4-1 μm

271  
272 Fig. 5i shows the absolute VIS-IR reflectance of all surfaces including fusion crust (A)  
273 and average spectra (Avg) of all internal meteorite surfaces (B-E). Fig. 5ii shows the normalized  
274 VIS-IR reflectance spectra of Mukundpura obtained normalizing the spectra at 0.55 μm for its  
275 corresponding phase angle the same normalization method used for spectral analysis of ONC-T

276 data [Tatsumi *et al.*, 2019]. The normalized spectra in Fig. 5ii are also resampled to the Hayabusa  
277 2 ONC-T spectral bands (ul: 0.40  $\mu\text{m}$ , b: 0.48  $\mu\text{m}$ , v: 0.55  $\mu\text{m}$ , Na: 0.59  $\mu\text{m}$ , w: 0.70  $\mu\text{m}$ , x: 0.86  
278  $\mu\text{m}$ , and p: 0.95  $\mu\text{m}$ ) [Tatsumi *et al.*, 2019] for the corresponding surfaces and phase angles. Fig.  
279 5iii is the color/visible slope plot between v-to-p slope ( $R_{0.55}/R_{0.95}$ ) and ul-to-v slope  
280 ( $R_{0.40}/R_{0.55}$ ) which helps to understand the visible color variations for different Mukundpura  
281 surfaces including the fusion crust and the different viewing geometries for each surface.

282 The VIS-IR spectra of CM chondrites are generally characterized by modestly blue- to  
283 red slopes and usually show a characteristic absorption band around  $\sim 0.7 \mu\text{m}$  associated with a  
284  $\sim 0.9\text{-}1.1 \mu\text{m}$  absorption band [Beck *et al.*, 2018; Cloutis *et al.*, 2011]. Cloutis *et al.* [2011]  
285 studied the VIS-IR spectral properties of 39 CM chondrites at viewing angles  $i = 30^\circ$  and  $e = 0^\circ$   
286 and found that in general overall slope of VIS-IR spectra range from blue-sloped to red-sloped  
287 with brighter spectra being more red-sloped and matrix-enriched CM spectra are more blue-  
288 sloped than bulk samples. The  $\sim 0.7 \mu\text{m}$  absorption feature is associated with  $\text{Fe}^{2+}$  and  $\text{Fe}^{3+}$   
289 charge transfer and the  $0.9 \mu\text{m}$  absorption band is attributed to  $\text{Fe}^{2+}$  crystal field transitions in Fe-  
290 bearing phyllosilicates within the CMs [Cloutis *et al.*, 2011]. The  $0.7 \mu\text{m}$  absorption band is also  
291 correlated with the amount of water and therefore related to the presence and abundance of  
292 phyllosilicates in the CMs studied [Beck *et al.*, 2018]. Also, there are correlation between  
293 reflectance value at  $0.55 \mu\text{m}$  and the carbon content in the CMs [Beck *et al.*, 2018; Cloutis *et al.*,  
294 2011].

295 *Fusion crust (Surface A; Fig. 5):* All VIS-IR spectra of fusion crust have weak broad  
296 convex spectral shape with the reflectance maximum centered on  $0.7 \mu\text{m}$  and the reflectance of  
297 0.05 for the overall spectral range (Fig. 5i A); except for phase angle  $50^\circ\text{-}50^\circ$  (Fig. 5i A: olive).  
298 Normalizing the fusion crust spectrum (Fig. 5ii A) enhances the convex shape for all phase  
299 angles showing the spectra is blue-sloped to red-sloped with the spectral inflection at  $0.7 \mu\text{m}$ ; in  
300 other words, the absence of the characteristic  $0.7 \mu\text{m}$  absorption band, suggesting the loss of  
301 water in the serpentines/phyllosilicates [Beck *et al.*, 2018] due to the atmospheric heating during  
302 the meteorite fall. The color slope plot for the fusion crust (Fig. 5iii A) shows that there are no  
303 considerable variations within the ul-to-v slope (blue slope) where the values are roughly  
304 concentrated around 0.3 suggesting that ul-to-v slope is not affected by varying viewing  
305 geometry for the fusion crust. However, v-to-p slope (red slope) in the slope plot (Fig. 5iii A)  
306 exhibits a slight linear behavior where the slope increases roughly with increase in phase  
307 angle/viewing geometry with the highest value of 0.05 (+ve) for phase angle  $50^\circ\text{-}50^\circ$  (Fig. 5iii A;  
308 olive) and least value of -0.12 for phase angle  $13^\circ\text{-}13^\circ$  (Fig. 5iii A; blue). It is important to note  
309 that, all v-to-p slope have negative values except for the value at phase angle  $50^\circ\text{-}50^\circ$  (Fig. 5iii A;  
310 olive). However, all spectra have a downturn behavior after  $0.85 \mu\text{m}$  which may correspond to  
311 contributions from Fe-bearing minerals such as Fe-poor phyllosilicates, Fe-cronstedtite, and/or  
312 Fe-olivine within the matrix/chondrules [Cloutis *et al.*, 2011].  
313



314

315 **Figure 5.** i) Absolute VIS-IR spectra, ii) Normalized spectra at 0.55  $\mu\text{m}$ , iii) spectral parameter  
 316 plot between v-to-p slope ( $\text{Ref}_{0.55}/\text{R}_{0.95}$ ) and ul-to-v slope ( $\text{Ref}_{0.40}/\text{Ref}_{0.55}$ ) for fusion crust (A),  
 317 intrinsic surfaces (B-E), and the average spectra of surfaces (B-E) for its varying viewing  
 318 geometry.  
 319

320

321

322 **4.2.1 Absolute VIS-IR spectra of Internal Mukundpura surfaces**

323 The absolute reflectance spectra of fresh Mukundpura surfaces (Fig. 5i B-E) shows that  
 324 reflectance behavior of surface B (Fig. 5i B) for varying viewing geometry for the corresponding  
 325 phase angles show only small variations except for phase angle 50°-50° (olive).

326 The reflectance spectra of surface C (Fig. 5i C) shows most variations among the phase  
 327 angles compared to rest of the surfaces B-E. The overall reflectance of the spectra obtained for  
 328 asymmetric viewing geometry and increasing phase angles have significantly linear behavior;  
 329 13°-13° (blue) > 13°-20° (orange) > 13°-30° (green) > 13°-40° (red) > 13°-50° (violet). However,  
 330 the symmetric viewing geometry with increasing phase angle (13°-13°, 20°-20°, 30°-30°, 40°-40°,  
 331 and 50°-50°) have only small differences in the reflectance values for the overall spectra. The  
 332 spectra show an increase in reflectance with different geometry and the highest reflectance is  
 333 obtained for phase angle 50°-50° with diagnostic change in slope (Fig. 5i C; olive). However, the  
 334 red-sloped spectral region until 0.8 μm increases slightly with increasing phase angles.

335 VIS-IR reflectance for surfaces D (Fig. 5i D) and E (Fig. 5i E) have very similar behavior  
 336 with nearly flat spectral shape and narrow linear variations in the reflectance values among the  
 337 different viewing geometry. The reflectance spectra at phase angle 50°-50° for surface E however  
 338 has the brightest spectrum and slightly stronger red-slope (Fig. 5i E; olive).

339

340 **4.2.2 Spectral Dependency on Phase Angle and Surface roughness**

341 Among normalized VIS-IR spectra for all surfaces (Fig. 5ii B-E), surface B shows  
 342 different spectral behavior than rest of the surfaces for all phase angles including the fusion crust  
 343 (Fig. 5ii B). Also, there is no particular trend between corresponding v-to-p slope and ul-to-v  
 344 slope for the normalized spectra of surface B (Fig. 5iii B). This behavior could be explained by  
 345 either surface B being matrix enriched compared to the other surfaces which would correspond  
 346 to bulk samples [*Cloutis et al.*, 2011], or it could be simply due to the intrinsic surface  
 347 roughness. For all phase angle observations, the v-to-p slope have negative values (red slope),  
 348 but the ul-to-p slope values spread from negative (red slope) to positive (blue slope) values,  
 349 which is also evident from the normalized surface B spectra in Fig. 5ii B). Importantly, spectra  
 350 of surface B for all phase angles have a weak absorption feature near 0.7 μm (attributable to  
 351 Fe<sup>2+</sup>-Fe<sup>3+</sup> charge transfer) and a IR downturn after 0.88 μm (ascribable to Fe<sup>2+</sup> d-d crystal field  
 352 transitions); both of these features suggests the presence of Fe-poor serpentines in the matrix  
 353 [*Cloutis et al.*, 2011]. These absorption features are also observed in the powdered sample of  
 354 Mukundpura meteorite in the study by *Izawa et al.* [2019].

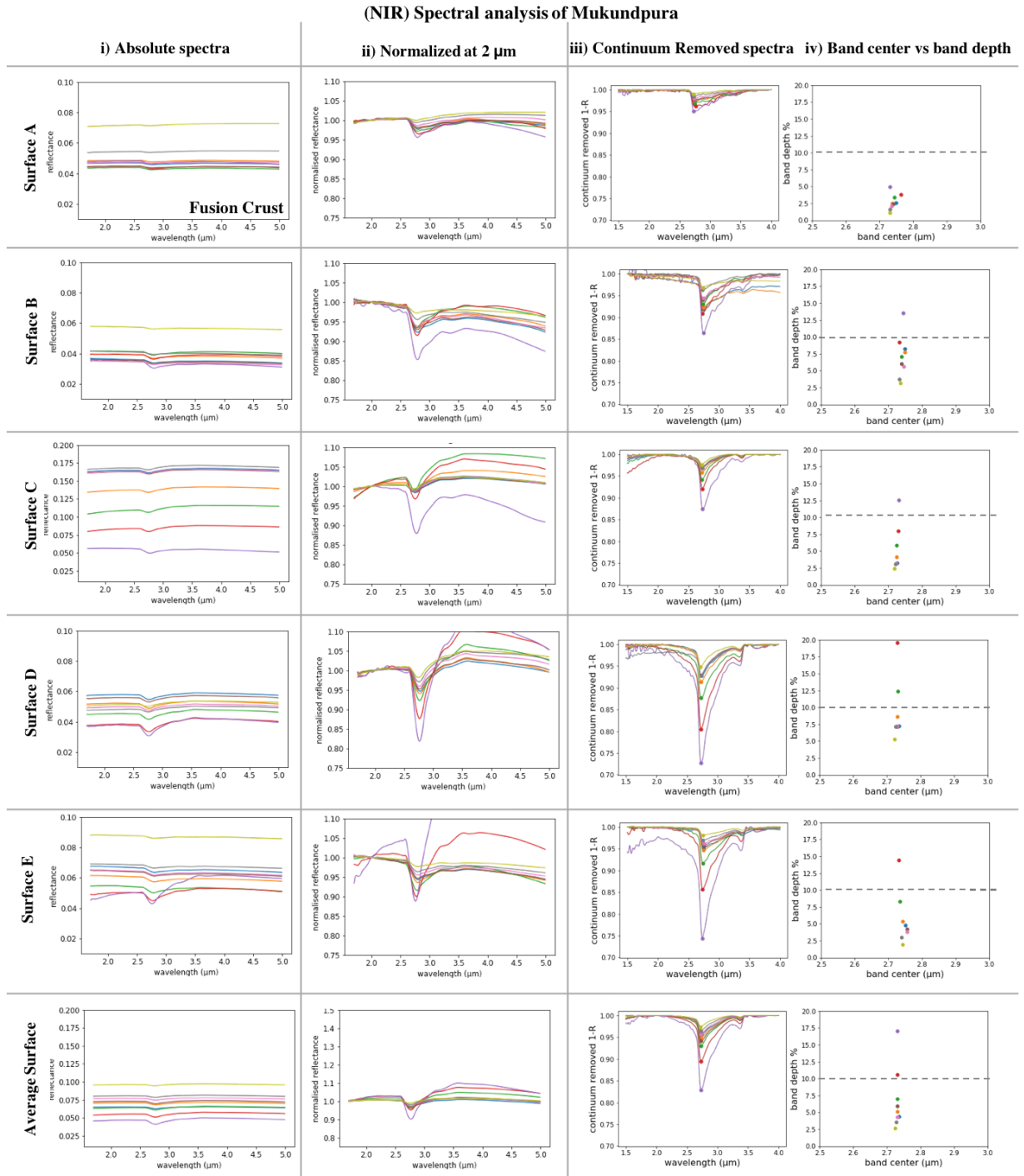
355 After normalization, the surfaces C-E shows very similar spectral shape for the  
 356 corresponding phase angle of each surface C, D, and E (Fig. 5ii C, D, E) irrespective of the  
 357 differences in the surface roughness among the surfaces. The spectral slope ul-to-v is positive  
 358 (blue-sloped) for all phase angles of all the three surfaces C, D, and E (Fig. 5ii C, D, E). On the  
 359 other hand, the v-to-p spectral slope shows a strong linear trend with the corresponding phase  
 360 angle observation for all the three surfaces C, D, E (Fig. 5ii C, D, E) whose values changes from  
 361 positive (red sloped) to negative (blue-sloped) in the order of decreasing phase angles for  
 362 symmetric viewing geometry and increasing phase angles for asymmetric viewing geometry;  
 363 50°-50° > 40°-40° > 30°-30° > 20°-20° > 13°-13° > 13°-20° > 13°-30° > 13°-40° > 13°-50°. It is also  
 364 interesting to note that in general cases v-to-p slope for symmetric viewing geometries (50°-50° >  
 365 40°-40° > 30°-30° > 20°-20° > 13°-13°) have positive values (blue-sloped) and v-to-p slope for the  
 366 asymmetric viewing geometries (13°-13° > 13°-20° > 13°-30° > 13°-40° > 13°-50°) have negative

367 values (red-sloped). All the spectra show IR downturn after 0.88  $\mu\text{m}$  which may correspond to  
368 Fe-bearing minerals [Cloutis *et al.*, 2011]. On the other hand, the 0.7  $\mu\text{m}$  absorption is not  
369 evident for all phase angles observations for surface C; however, a minor feature could be traced  
370 for surfaces D and E for phase angles say 13°-40° (Fig. 5ii D, E; red) and 13°-50° (Fig. 5ii D, E;  
371 violet). Unlike surface B which has both 0.7 and 0.9  $\mu\text{m}$  absorption feature suggesting a matrix-  
372 enriched surface and/or with Fe-bearing hydrous minerals, the behavior of evident IR downturn  
373 after 0.88  $\mu\text{m}$  with weak or no 0.7  $\mu\text{m}$  absorption features for surfaces C, D, E may correspond  
374 to the surface containing bulk representation of matrix and chondrules containing crystalline  
375 anhydrous minerals (possibly Fe-bearing olivine within the chondrules) along with Fe-poor  
376 serpentines within the matrix [Cloutis *et al.*, 2011].  
377

### 378 **4.3 Near Infrared (NIR): 1 – 5 $\mu\text{m}$**

379 NIR spectroscopy is sensitive to the presence OH and H<sub>2</sub>O groups within the rocks and  
380 allows inferring the mineralogy of hydrated/hydrous carbonaceous chondrites [Beck *et al.*, 2010;  
381 Farmer, 1974; Hamilton *et al.*, 2019; Hiroi *et al.*, 1996; Matsuoka *et al.*, 2019]. One of the  
382 characteristic spectral parameter of CM chondrites in the NIR spectral region is the presence of  
383 diagnostic sharp asymmetric absorption feature near the 3  $\mu\text{m}$  water/OH absorption band. The  
384 strength of the band is due to the combination of stretching  $\nu_1$  and anti-stretching  $\nu_3$  vibration  
385 modes of water (H<sub>2</sub>O) [Beck *et al.*, 2010]. The position of band minima (band center at maximum  
386 absorption) at 3  $\mu\text{m}$  feature is attributed to the stretching vibrations of the hydroxyl groups in the  
387 octahedral layer of phyllosilicates probing the local cationic environment (tetrahedral cations)  
388 [Ryskin, 1974]; the band minima at 2.72  $\mu\text{m}$  corresponds to Mg-OH and the band minima at 2.82  
389  $\mu\text{m}$  corresponds to Fe-OH [Beck *et al.*, 2018; Beck *et al.*, 2010; Cloutis *et al.*, 2011; Hiroi *et al.*,  
390 1996; McAdam *et al.*, 2015; Takir *et al.*, 2013]. The 3  $\mu\text{m}$  band is usually accompanied by the  
391 second narrow reflectance minimum around 2.95  $\mu\text{m}$ . The shape of this 3  $\mu\text{m}$  is attributed to the  
392 chemistry of the phyllosilicates and mineralogy of the samples [Beck *et al.*, 2010; Browning *et*  
393 *al.*, 1996; Howard *et al.*, 2009; Takir *et al.*, 2013]. Weaker absorption features around 3.4-3.5  
394  $\mu\text{m}$  and sometimes at 2.3  $\mu\text{m}$  is attributed to Mg-OH in serpentines and C-H stretching from  
395 organics [Beck *et al.*, 2018]. The presence of a reflectance minimum around 3.1  $\mu\text{m}$  is commonly  
396 attributed to adsorbed water [Beck *et al.*, 2010].  
397

398 Absolute NIR spectra of all the surfaces including the fusion crust of Mukundpura  
399 sample studied (Fig. 6i) show nearly feature-less spectra overall except with the prominent 3  $\mu\text{m}$   
400 absorption feature. In order to better understand the relation of phase angle observations and  
401 surface roughness on the band shape and band center, we take a closer look at the following  
402 spectral parameters; a) normalized spectra where the reflectance at 2  $\mu\text{m}$  is normalized to one  
403 (Fig. 6ii); to better understand the minor slope changes with respect to phase angle and surface  
404 roughness, b) continuum removed spectra with continuum shoulders at 1.5 and 4  $\mu\text{m}$  to derive  
405 the spectral parameters of diagnostic absorption feature at 3  $\mu\text{m}$ , c) the band center vs band  
406 depth; to quantitatively understand the nature of 3  $\mu\text{m}$  spectral feature (Fig. 6iv), their  
407 corresponding clay mineralogy, and their spectral dependency on phase angle of observation and  
408 surface roughness.



I(13°)-R(13°)  
 I(13°)-R(20°)  
 I(13°)-R(30°)  
 I(13°)-R(40°)  
 I(13°)-R(50°)  
I(20°)-R(20°)  
 I(30°)-R(30°)  
 I(40°)-R(40°)  
 I(50°)-R(50°)

408  
 409 **Figure 6.** i) Absolute NIR spectra, ii) Normalized spectra at 2.0μm, iii) continuum  
 410 removed spectra between 1.5 and 4 μm, iv) spectral parameter plot between 3 μm band  
 411 center and absorption band depth for fusion crust (A), intrinsic surfaces (B-E), and the average  
 412 spectra of surfaces (B-E) for its varying viewing geometry.

413

414 *Fusion crust (Fig. 6ii-iv A)*: The normalized NIR spectra of the fusion crust (Fig. 6ii A)  
415 show that the strength of the 3  $\mu\text{m}$  is highly subdued and varies with phase angle of observation.  
416 The normalized spectra (Fig. 6ii A) for phase angle 50°-50° is nearly flat (Fig. 6ii A; olive) with  
417 weak absorption near 3  $\mu\text{m}$ , whereas the phase angles 13°-40° (Fig. 6ii A; red) and 13°-50° (Fig.  
418 6ii A; violet) have stronger 3  $\mu\text{m}$  along with weak absorption features around 3.4  $\mu\text{m}$  confirming  
419 the presence of Mg-serpentine and C-H stretching [Beck *et al.*, 2018] of organics and also have  
420 a negative spectral slope after 4  $\mu\text{m}$ . The continuum removed spectra (Fig. 6iii A) shows the  
421 highly asymmetrical 3  $\mu\text{m}$  absorption band and the band-center vs band-depth plot (Fig. 6iii A)  
422 shows that the band center of the 3  $\mu\text{m}$  features centers around 2.72-2.75  $\mu\text{m}$  with < 2%  
423 absorption for most phase angles with the exception of 2-5% absorption for phase angles 13°-30°  
424 (Fig. 6iv A; green), 13°-40° (Fig. 6iv A; red) and 13°-50° (Fig. 6iv A; violet). The weak 3  $\mu\text{m}$   
425 absorption feature of fusion crust is attributed to the loss of water (OH) due to the atmospheric  
426 heating during entry; and the 2.72  $\mu\text{m}$  is attributed to the loss of water within the Mg-serpentine.

427 *Mukundpura surface (Fig. 6ii-iv B-E)*: The normalized NIR spectra (Fig. 6iii B-E) shows  
428 that the spectral slope and shape is highly dependent on the phase angle and the surface  
429 topography. The normalized NIR spectra of surface B (Fig. 6iii B) at all phase angles have a  
430 slight negative slope at all NIR wavelengths; however, the remaining surfaces (Fig. 6iii C-E)  
431 have positive slope upto 3.5  $\mu\text{m}$  and a negative slope afterwards (3.5-5  $\mu\text{m}$ ). Such differences are  
432 not obvious in the not normalized spectra (Fig. 6ii B-E). Among the phase angle of observations  
433 for all surfaces, the normalized spectra for phase angles 13°-40° (Fig. 6ii B-E; red) and 13°-50°  
434 (Fig. 6ii B-E; violet) show the strongest spectral shape and features such as spectral slopes and  
435 absorption strength. Spectra for phase angles 50°-50° (Fig. 6iv B-E; olive) have the least contrast  
436 in spectral shape and features. The continuum removed spectra (Fig. 6iii B-E) and the band  
437 center vs band depth at 3  $\mu\text{m}$  plot (Fig. 6iii B-E) of all fresh Mukundpura surfaces for all phase  
438 angles and surface roughness displays evident narrow asymmetric absorption feature with a band  
439 center around 2.72  $\mu\text{m}$ . It remains almost constant irrespective of varying surface roughness and  
440 phase angles (Fig. 6iii-iv B-E) and this band position corresponds to the Mg-OH stretching  
441 modes observed in Mg-phylosilicates [Beck *et al.*, 2010; Takir *et al.*, 2013]. However, the  
442 strength of these absorption features varies with respect to phase angle of observation whose  
443 values are generally less than 10% (Fig. 6iv B-E) except for phase angles 13°-40° (Fig. 6iv B-E;  
444 red) and 13°-50° (Fig. 6iv B-E; violet) which have strongest absorptions in some cases up to 27%  
445 (Fig. 6iii D; violet). On careful examination, the minor spectral inflection showing the evidence  
446 of a weak 2.95  $\mu\text{m}$  absorption accompanying the strongest ~2.72  $\mu\text{m}$  absorption feature is  
447 evident for the continuum removed NIR spectra at phase angles 13°-40° (Fig. 6iii B-E; red) and  
448 13°-50° (Fig. 6iii B-E; violet). The continuum removed spectra for all surfaces (Fig. 6iii B-E)  
449 also displays a weaker but evident ~3.4  $\mu\text{m}$  absorption feature for all phase angles with the  
450 strongest features for 13°-40° (Fig. 6iii B-E; red) and 13°-50° (Fig. 6iii B-E; violet), further  
451 confirming the presence of Mg-serpentine in the Mukundpura sample studied. The absence of  
452 any ~3.1  $\mu\text{m}$  band for all NIR spectra of surfaces and fusion crust confirms that there is no  
453 adsorbed water [Beck *et al.*, 2010] in the meteorite surfaces and the measurements are taken in  
454 vacuum conditions.

455 The NIR region shows that the band absorption strength for 2.72  $\mu\text{m}$  is highly dependent  
456 on the phase angle of observation and surface flatness/roughness. This must be carefully taken  
457 into consideration while performing quantitative analysis such as correlating the shape and  
458 strength of the 3  $\mu\text{m}$  absorption band to characterize the level of hydration [Beck *et al.*, 2014;

459 *Garenne et al., 2016; Garenne et al., 2014*] when analyzing the remote sensing/landed surface  
460 spectral data of carbonaceous asteroids as Ryugu and Bennu.

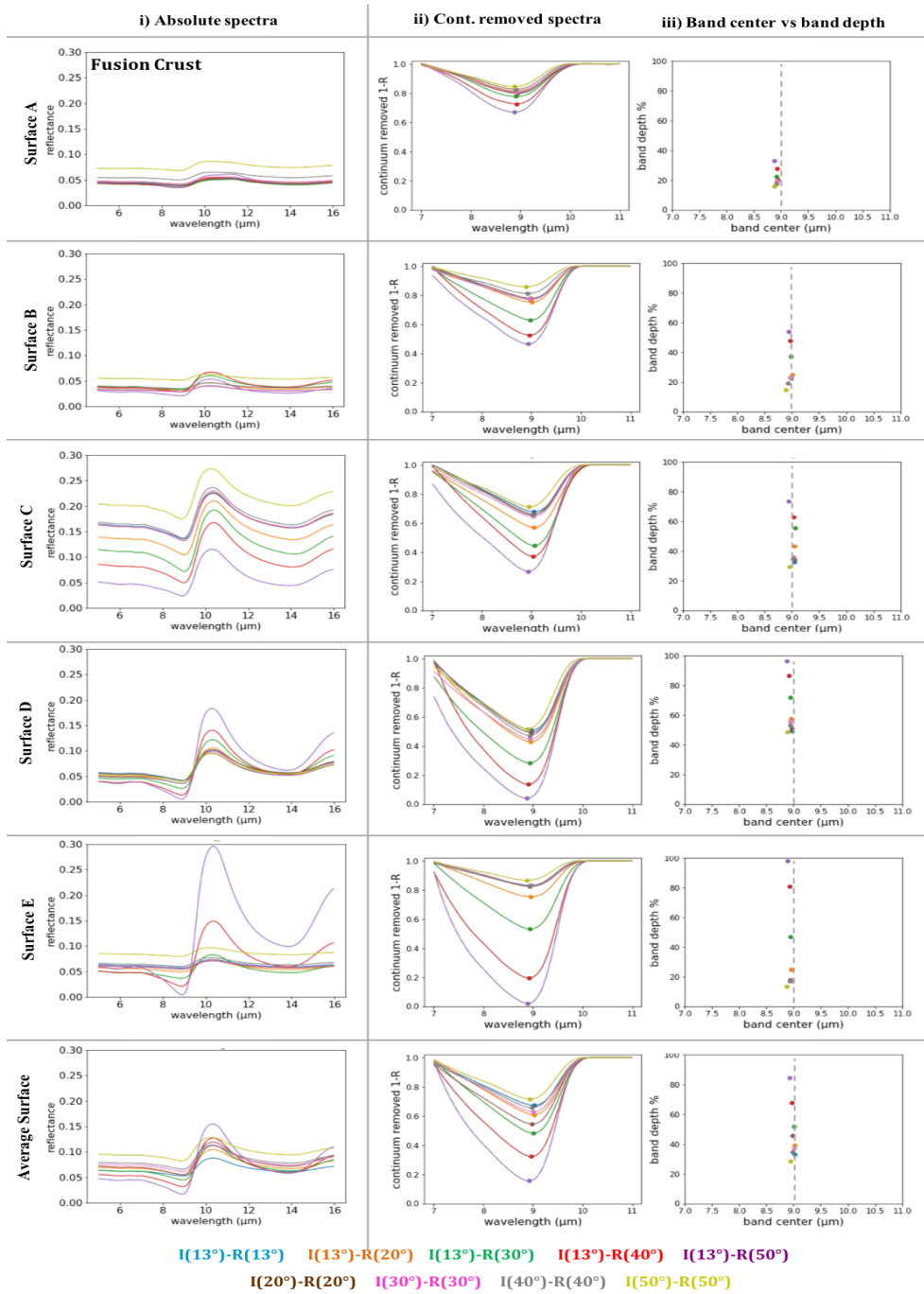
461

#### 462 **4.4 Mid Infrared (MIR): 5-16 $\mu\text{m}$**

463 The spectral band shape and position in the MIR region is widely studied for the  
464 evidence of the presence and nature of phyllosilicates, their hydrous alteration state, and  
465 therefore gives information on the initial composition of anhydrous minerals in the meteorite  
466 [*Howard et al., 2009, 2011; Tomeoka and Buseck, 1985*]. When the primitive meteorites alter,  
467 the first Fe-matrix of the anhydrous silicates convert to phyllosilicates and then the Mg-rich  
468 silicates within the chondrules starts to alter as the process progresses [*McAdam et al., 2015*].  
469 The late stage of alteration therefore tends to produce predominantly Mg-rich serpentines  
470 [*McAdam et al., 2015*]. The phyllosilicate alteration phases of CM chondrites are mostly  
471 composed of various serpentines [*Barber, 1981; Glotch et al., 2007; Hanowski and Brearley,*  
472 *2001; Laurretta et al., 2000; MacKinnon, 1982; Richardson, 1981; Zega and Buseck, 2003;*  
473 *Zolensky et al., 1993*].

474 Reflectance spectra of surfaces A-E (Fig. 7i; A-E): The MIR spectrum (5-16  $\mu\text{m}$ ) of all  
475 surfaces of Mukundpura sample possess three characteristic spectral features; a) sharp  
476 Christiansen Feature (CF) minimum centered near  $\sim 9 \mu\text{m}$ , b) reflectance maximum centered near  
477  $10.5 \mu\text{m}$ , and c) broad absorption feature extending from 10-16  $\mu\text{m}$  with the center around 14  
478  $\mu\text{m}$ . However, the strength and the nature of these bands vary with respect to the surface  
479 roughness and the phase angle combinations. The stronger spectral shape for all different  
480 surfaces is observed in the spectra taken at phase angle of  $13^\circ$ - $40^\circ$  (Fig. 7i C-E; red) and  $13^\circ$ - $50^\circ$   
481 (Fig. 7i C-E; violet) whereas the weakest spectral shape is attributed to the observations made at  
482 phase angle  $50^\circ$ - $50^\circ$  (Fig. 7i C-E; olive).

(MIR) Spectral analysis of Mukundpura



483  
 484 **Figure 7.** i) Absolute MIR spectra, ii) continuum removed spectra between 7 and 11  $\mu\text{m}$ , iii)  
 485 spectral parameter plot between 9  $\mu\text{m}$  band center and absorption band depth for fusion crust (A),  
 486 intrinsic surfaces (B-E), and the average spectra of surfaces (B-E) for its varying viewing  
 487 geometry.

488  
 489 The spectral shape of the Mukundpura sample and their characteristic spectral features,  
 490 CF minimum at 9  $\mu\text{m}$  and the reflectance maximum at  $\sim 10.5 \mu\text{m}$ , are attributed to the stretching  
 491 modes of  $\text{SiO}_4$  bonds in serpentine, specifically resembling Mg-serpentine sample, Burminco

492 from Mariposa County, CA, USA (BUR-1690;  $(\text{Mg}_{2.81}\text{Fe}_{0.35})(\text{Si}_{1.87}\text{Al}_{0.07})\text{O}_5(\text{OH})_4$ ) in the  
 493 spectroscopy study by *Glotch et al.* [2007] and therefore spectrally confirming the presence of  
 494 dominant Mg-serpentine in the matrix of Mukundpura, which is also suggested in the study by  
 495 *Haberle et al.* [2019].

496 In order to study the dependency of Christiansen feature minimum ( $\sim 9 \mu\text{m}$ ) for its  
 497 spectral parameters such as band center vs band depth (Fig. 7iii; A-E) in relation to observations  
 498 at varying phase angle and surface roughness, we first performed continuum removal of the  
 499 spectra by fitting the convex-hull over the  $9 \mu\text{m}$  absorption feature by anchoring the continuum  
 500 end points at reflectance values at  $7$  and  $11 \mu\text{m}$  (See Section 3.1.1 for methods) as shown in  
 501 Fig. 7ii; A-E, average spectra). For all the surfaces including the fusion crust, the continuum  
 502 removed spectra of all meteorite surfaces (Fig. 7ii; A-E) for the phase angle combinations  $13^\circ$ -  
 503  $30^\circ$  (Fig. 7A-E; green),  $13^\circ$ - $40^\circ$  (Fig. 7A-E; red) and  $13^\circ$ - $50^\circ$  (Fig. 7A-E; violet) shows strongest  
 504 band absorption whereas  $50^\circ$ - $50^\circ$  (Fig. 7A-E; olive) shows the weakest absorption at  $9 \mu\text{m}$ .

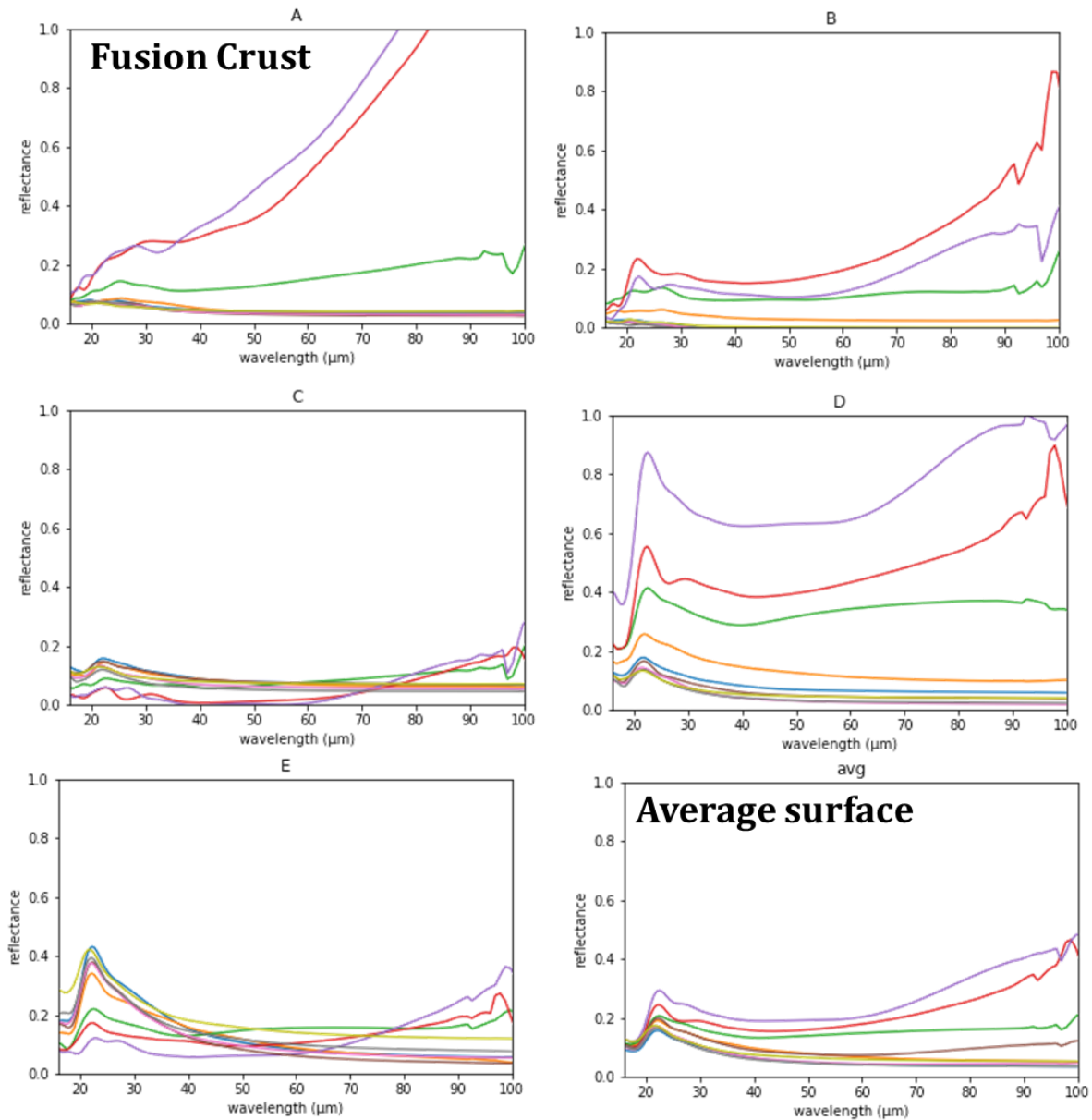
505 The band center versus band depth values plotted at Fig. 7iii (A-E) are calculated by  
 506 finding the band minima and the band depth at  $\sim 9 \mu\text{m}$  in the corresponding continuum spectra  
 507 (See Section 3.1.2 for methods). Fig. 7iii (A-E) shows that irrespective of the phase angle of  
 508 observation and the surface roughness, the band center for all the surfaces (Fig. 7iii B-E)  
 509 including the thermally altered fusion crust (Fig. 7iii A) is unchanged and centered at  $\sim 9 \mu\text{m}$ .  
 510 Therefore, the band center value at  $9 \mu\text{m}$  spectral parameter acts as a stable spectral parameter  
 511 that could be used to trace the presence of serpentines across the remote sensing targets. On the  
 512 other hand, the absorption band depth at  $9 \mu\text{m}$  is affected by thermal alteration (fusion crust;  
 513 Fig. 7iii-A) and viewing angles (Fig. 7iii; A-E). It is important to note that, for any surface the  
 514 band depths have extreme (high) values for phase angles at  $13^\circ$ - $30^\circ$  (Fig. 7i B-E; green),  $13^\circ$ - $40^\circ$   
 515 (Fig. 7i B-E; red) and  $13^\circ$ - $50^\circ$  (Fig. 7i B-E; violet); however, for other phase angles the band  
 516 depths don't have significant variations. This is important because at extreme viewing angle  
 517 remote sensing observations of asteroid targets such as Ryugu (Hayabusa2) and Bennu (OSIRIS-  
 518 REx), the band depth of the spectra should be carefully used for quantitative interpretation such  
 519 as abundance of phyllosilicates/serpentine [Maturilli et al., 2016; Potin et al., 2019]. This  
 520 behavior is also seen in the thermally altered fusion crust (Fig. 7iii A); however, the band depths  
 521 are subdued for all phase angles due to loss OH in the structure of serpentines.

522 Except for the MIR spectra of fusion crust (Fig. 7i; A), all the surface spectra (Fig. 7i; B-  
 523 E, Avg) shows a minor broad absorption feature near  $6 \mu\text{m}$  feature which is pronouncedly  
 524 present in the phase angles  $13^\circ$ - $40^\circ$  (Fig. 7i B-E; red) and  $13^\circ$ - $50^\circ$  (Fig. 7i B-E; violet), which is  
 525 also evidently visible in the average surface spectra (Fig. 7i; Avg). This  $6 \mu\text{m}$  absorption feature  
 526 is attributed to presence of bending modes of water molecules, specifically interlayer water of  
 527 the clay minerals [Beck et al., 2010; Garenne et al., 2014], Mg-serpentine in the case of  
 528 Mukundpura.

529

#### 530 **4.5 Far Infrared (FIR): 16-100 $\mu\text{m}$**

531 The FIR region of Mukundpura sample shows very complex spectral behavior with  
 532 respect to roughness and phase angle of measurement. The measurements at phase angles  $13^\circ$ - $40^\circ$   
 533 (Fig. 8B-E; red) and  $13^\circ$ - $50^\circ$  (Fig. 8B-E; violet) shows a very broad absorption feature extending  
 534  $22$ - $90 \mu\text{m}$ , and the strength of this absorption varies with surface roughness eg., surface Fig. 8 (C,  
 535 D, E). This absorption feature is not evident in remaining phase angle observations with the  
 536 nearly flat and dark spectra.

**(FIR) Spectrum of Mukundpura**

537  
538  
539  
540

**Figure 8.** FIR spectra of fusion crust (A), intrinsic surfaces (B-E), and the average spectra of surfaces (B-E) for its varying viewing geometry

541 *Surfaces B-E (Fig. 8B-E):* Irrespective of phase angle and surface roughness, all FIR  
542 spectra in the 16-60  $\mu\text{m}$  spectral range have two characteristic spectral features of CM  
543 meteorites; a minor reflectance peak near 16  $\mu\text{m}$  attributable to the librations of Mg-OH  
544 molecules within the octahedral sheet of 1:1 phyllosilicates [Farmer, 1974] and a sharp  
545 reflectance peak centered near  $\sim 22 \mu\text{m}$  corresponds to the bending modes of  $\text{SiO}_4$  [Farmer, 1974;

546 *Haberle et al.*, 2019]. These two distinct spectral features strongly indicate the presence of  
 547 abundant Mg-serpentine within Mukundpura, which is also observed in the study by *Haberle et*  
 548 *al.* [2019].

549 *Fusion Crust A* (Fig. 8A): The two spectral features centered near 16  $\mu\text{m}$  (absorption) and  
 550 22  $\mu\text{m}$  (peak) are highly subdued in the FIR spectra of the fusion crust (Fig. 8A), indicating the  
 551 dehydration/loss of volatiles during the atmospheric entry of the meteorite fall. Also, the FIR  
 552 spectra of fusion crust at phase angles 13°-40° (Fig. 8A; red) and 13°-50° (Fig. 8A; violet) display  
 553 very strong redder spectral slope after 30  $\mu\text{m}$ . In the remaining phase angle combinations, the  
 554 spectra are nearly flat and dark.

555

## 556 **5 Discussions**

### 557 **5.1 UV-FIR spectroscopy of Mukundpura**

#### 558 **5.1.1 Mineralogy**

559 Irrespective of the surface roughness and viewing geometry, all Mukundpura surfaces  
 560 have characteristic spectral features that help us in deciphering their bulk mineralogy.

561 In the UV-VIS region (0.25 – 0.6  $\mu\text{m}$ ), both fusion crust (Fig. 4A) and the meteorite  
 562 surfaces (Fig. 4B-E) exhibits carbon Fresnel peak ( $\text{sp}^2 \pi-\pi^*$ ) near 0.275  $\mu\text{m}$  [*Applin et al.*, 2018]  
 563 along with flat spectra in the visible region 0.325-0.6  $\mu\text{m}$  with reflectance values less than 0.1 for  
 564 all surfaces indicating the presence to nanophase graphite or amorphous carbon in the matrix  
 565 [*Applin et al.*, 2018].

566 In the VIS-IR region (0.4 – 1.0  $\mu\text{m}$ ; Fig. 5), the fresh interiors of Mukundpura sample for  
 567 surface B have a minor absorption feature near 0.7  $\mu\text{m}$  (attributable to  $\text{Fe}^{2+}$ - $\text{Fe}^{3+}$  charge transfer)  
 568 and amount of water within the CM and a downturn after 0.88  $\mu\text{m}$  (ascribable to  $\text{Fe}^{2+}$  d-d crystal  
 569 field transitions) indicating the presence of Fe-poor serpentines in the matrix [*Cloutis et al.*,  
 570 2011]. However VIS-IR spectra of surfaces C-E have evident IR downturn after 0.88  $\mu\text{m}$  with  
 571 weak or no 0.7  $\mu\text{m}$  absorption features and may correspond to the surface containing bulk  
 572 representation of matrix and chondrules containing crystalline anhydrous minerals (possibly Fe-  
 573 bearing olivine within the chondrules) along with Fe-poor serpentines within the matrix [*Cloutis*  
 574 *et al.*, 2011]. VIS-IR spectra of the fusion crust having a concave shape extending the entire VIS-  
 575 IR spectral region with no absorption at 0.7  $\mu\text{m}$  indicates the loss of water due to atmospheric  
 576 heating and back-transformation of hydrous mineralogy to their anhydrous counterparts.

577 NIR spectral region (1.5-5  $\mu\text{m}$ ) of fresh interiors of all Mukundpura surfaces (Fig. 6; B-  
 578 E) have the fundamental asymmetric spectral absorption feature associated with the hydroxyl  
 579 ( $\text{OH}^-$ ) band centered at 2.72  $\mu\text{m}$  supporting the presence of Mg-serpentines in its matrix. NIR  
 580 spectra of the fusion crust also possess the weak 3  $\mu\text{m}$  band centered near 2.7  $\mu\text{m}$  indicating the  
 581 potential survivability of some hydrous mineralogy within the matrix.

582 MIR spectral region (5-16  $\mu\text{m}$ ) of fresh Mukundpura surfaces (B-E) in Fig. 7 show that  
 583 all the internal Mukundpura surfaces exhibit the characteristic CF minimum indicative of  
 584 fundamental stretching modes of  $\text{SiO}_4$  with their band center at 9  $\mu\text{m}$  followed by reflectance  
 585 peak near 16  $\mu\text{m}$  indicator of librations of Mg-OH bonds. This further confirms the presence of  
 586 Mg-rich serpentines in their matrix. The fusion crust spectra however exhibit the CF minimum  
 587 slightly short-ward to 9  $\mu\text{m}$  with very weak 16  $\mu\text{m}$  peak, which indicates the formation of  
 588 anhydrous minerals.

589 All FIR spectra (16-100  $\mu\text{m}$ ) of the intrinsic Mukundpura surfaces (Fig. 8; B-E) have the  
 590 sharp reflectance peak near 22  $\mu\text{m}$  which is the fundamental bending modes of  $\text{SiO}_4$  in the  
 591 aqueously altered minerals which is associated with the stretching modes of  $\text{SiO}_4$  in the MIR

592 spectral region. FIR spectra of the fusion crust also possess the 22  $\mu\text{m}$  spectral but weaker and  
593 broader indicating the presence of preferably anhydrous counterparts of Mg-serpentine such as  
594 Mg-olivine and pyroxene.

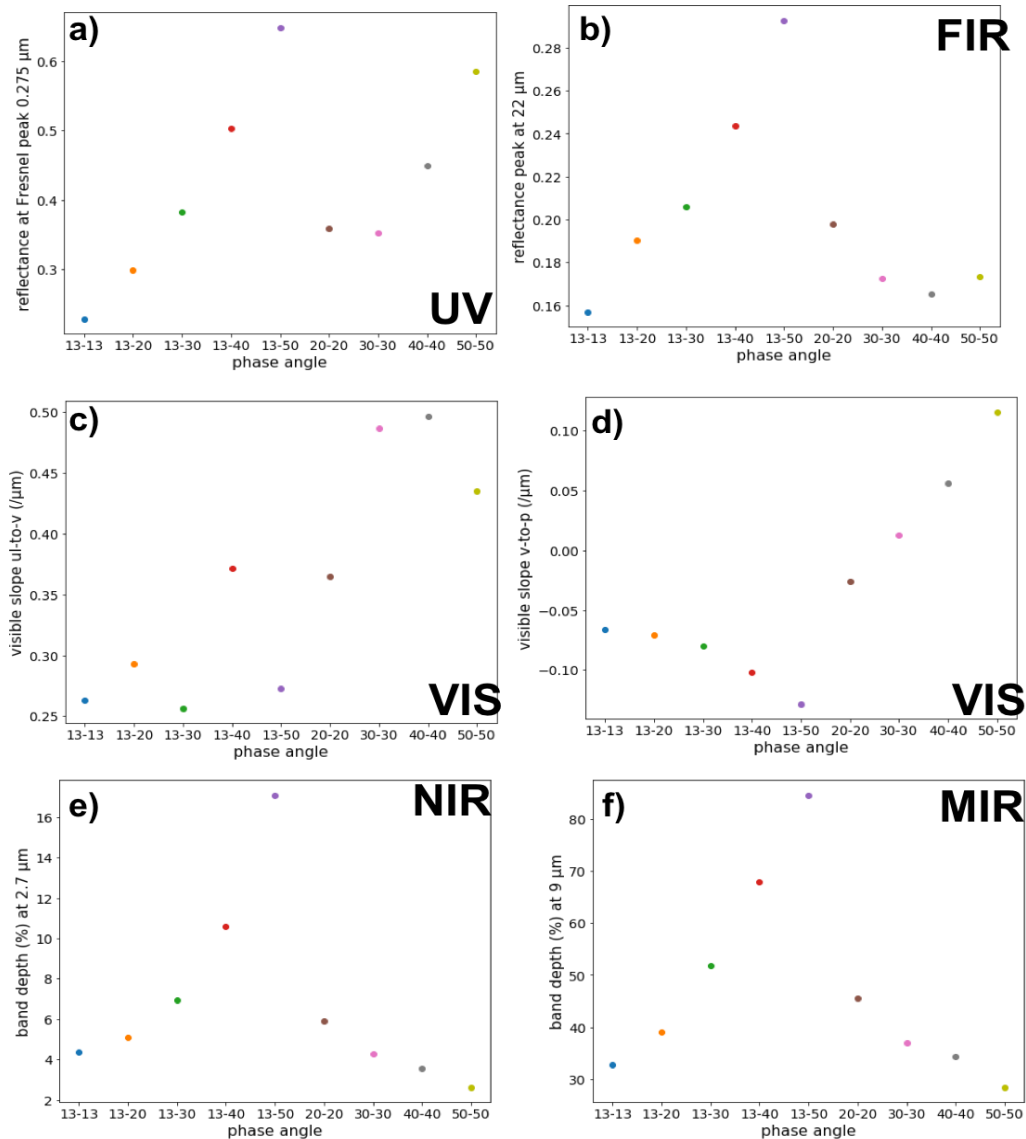
595 Overall, the carbon rich matrix along with the dominant presence of Mg-serpentine can  
596 be interpreted from the spectroscopy of the studied Mukundpura sample, along with the thermal  
597 alteration effects in the spectra of the fusion crust. Mukundpura sample studied appears to have  
598 very homogeneous bulk mineralogy for all the intrinsic surfaces.

599

### 600 **5.1.2 Dependency on Viewing Geometry**

601 The observations by Hayabusa2 and OSIRIS-REx show that the surfaces of both Ryugu  
602 and Bennu are not covered by regolith or fine dust but instead rocks of size similar to our  
603 Mukundpura fragment. This makes our study on viewing geometries especially relevant, as in  
604 the past typically all similar studies have been performed on powders.

605 This study shows that the spectral parameters such as brightness, slope, and absorption  
606 band centers of CM-type Mukundpura meteorite is highly influenced by the respective viewing  
607 geometry but behaves systematically for the respective spectral range irrespective of the 3D  
608 surface roughness for the compositionally homogeneous surface. In order to understand the  
609 general CM/Mukundpura spectral characteristics with respect to symmetrically and  
610 asymmetrically changing viewing geometry, the behavior of spectral parameters of average  
611 surface of Mukundpura is plotted against the varying geometry in Fig. 9.

**Spectral parameter vs Phase Angle**

612  
 613 **Figure 9.** Relationship between symmetric and asymmetrically varying phase angle  
 614 behavior with respect to UV-FIR spectral parameters derived from average surface spectra of  
 615 Mukundpura meteorite studied; a) phase angle vs reflectance at UV fresnel peak of average  
 616 surface spectra in Fig. 4, b) phase angle vs FIR reflectance peak at bending modes of SiO<sub>2</sub> of  
 617 average surface spectra in Fig. 8, c) phase angle vs VIS slope (ul-to-v) from average surface  
 618 spectra in Fig. 5, d) phase angle vs VIS slope (v-to-p) from average surface spectra in Fig. 5, e)  
 619 phase angle vs NIR band depth of water band at ~2.8 μm measured from average surface spectra  
 620 in Fig. 6, and f) phase angle vs MIR band depth of reflectance minimum at ~9 μm measured  
 621 from average surface spectra in Fig. 7.

622

623 *UV-VIS spectral region (0.25 – 0.6 μm):* Fig. 9a shows that for both asymmetrically and  
 624 symmetrically increasing viewing geometries, the reflectance value at Fresnel peak near ~0.275  
 625 μm increases with increasing phase angle. It is also important to note that, the viewing geometry

626 with similar reflectance angle irrespective of the incidence angle have similar reflectance values  
627 at Fresnel peak (except for angle 20°-20°). It can be summarized as the reflectance value at the  
628 carbon Fresnel peak (~0.275 μm) decreases with decreasing reflectance angle in the order; 13°-  
629 50°, 50°-50°) > (13°-40°, 40°-40°) > (13°-30°, 30°-30°) > (13°-20°, 20°-20°) > (13°-13°). Therefore,  
630 for the spectroscopy of CM-petrology type or any C-type asteroids surfaces in the UV spectral  
631 region, irrespective of the foot-print of observation which is influenced by varying incidence  
632 angles and 3D surface roughness, the reflectance value at the carbon Fresnel peak is only  
633 dependent on the viewing angle/reflectance angle.

634 *VIS-IR spectral region (0.4 – 1.0 μm)*: The behavior of visible spectral slopes ul-to-v and  
635 v-to-p for symmetrically and asymmetrically varying viewing angles is shown in Fig. 9c and Fig.  
636 9d respectively. Fig. 9c shows no particular correlation among the viewing geometries for  
637 spectral slope ul-to-v for both symmetrically and asymmetrically varying phase angles. Whereas  
638 spectral slope v-to-p shows a systematic behavior with changing viewing geometry, where slope  
639 decreases with asymmetrically increasing phase angle and increases with symmetrically  
640 increasing phase angles. It can also be safely interpreted as v-to-p slope is positive for symmetric  
641 phase angles and negative for asymmetric phase angles. Therefore, our analysis suggests that the  
642 viewing geometry should be carefully considered while interpreting the spectral slopes in the  
643 remotely sensed C-type asteroids such as ONC-T data of Ryugu surface.

644 *NIR & MIR spectral region (1.5 – 16.0 μm)*: In the NIR region, the 3 μm hydroxyl (OH-)  
645 absorption band is the characteristic spectral feature of C-type asteroids which indicates the  
646 nature and abundance of aqueously altered minerals in the surface. Whereas in the MIR region,  
647 the CF minimum is the characteristic spectral feature of CMs to characterize the nature and  
648 crystallinity of the silicate mineralogy. The band depth at 2.7 μm band and 9 μm absorption  
649 features for NIR and MIR spectral region is plotted in Fig. 9e and Fig. 9f for the symmetrically  
650 and asymmetrically varying viewing geometry. Fig. 9e, f shows that the band depths of these  
651 spectral absorption show similar behavior where the slope increases with asymmetrically  
652 increasing phase angle and decreases with symmetrically decreasing phase angles.

653 The absorption band depth significantly increases with increasing phase angles for the  
654 asymmetric viewing geometry in the order 13°-13° < 13°-20° < 13°-30° < 13°-40° < 13°-50° could  
655 be explained by spectral mixing of different minerals having different phase curves near 3 μm  
656 absorption band and 9 μm absorption band for the particular footprint/surface within the CM  
657 chondrite studied (as incidence angle is fixed). For asymmetric phase angles with fixed incidence  
658 angle, at low phase angles, the strong contributions from most materials is reflected and therefore  
659 weakens the absorption band. Whereas at higher phase angles the materials with lesser  
660 reflectance at large scattering angles do not contribute to the reflected signal and therefore  
661 enhances the absorption depth of 3 μm and 9 μm band. This may suggest that the water band and  
662 CF band for the hydrous minerals within the CMs is not affected by viewing geometry. This  
663 explanation is further supported by absolute reflectance of the spectra for all surfaces of the  
664 meteorite studied in Fig. 6i where the overall NIR reflectance of the spectra decreases with  
665 increasing phase angle for the asymmetric viewing geometry for all surfaces which is a reverse  
666 behavior to the absorption band center at 3 μm. This behavior can be traced for the overall MIR  
667 reflectance spectra in Fig. 7i. However, the absorption band strength for symmetric viewing  
668 geometry decreases with increasing phase but not significantly (Fig. 9 e, f). Also, the overall  
669 reflectance of the absolute spectra for all the surfaces for symmetric viewing geometry does not  
670 vary significantly (Fig. 6i; NIR and Fig. 7i; MIR). For all the surfaces the absorption band

671 strength for both 3  $\mu\text{m}$  (Fig. 6iii, Fig. 9e) and 9  $\mu\text{m}$  (Fig. 7ii, Fig. 9f) absorption band is largest  
 672 for viewing geometry 13°-50° and is least for viewing geometry 50°-50°.

673 *FIR spectral region (16 – 100  $\mu\text{m}$ ):* The FIR spectral behavior with respect to viewing  
 674 geometry is highly influenced by the respectively surface roughness and texture (Fig. 8). In order  
 675 to understand the general FIR spectral characteristics for varying viewing geometry, the  
 676 reflectance peak near 22  $\mu\text{m}$  for average surface spectra is plotted against the symmetrically and  
 677 asymmetrically varying viewing geometry in Fig. 9b. Fig. 9b shows that the reflectance peak  
 678 near 22  $\mu\text{m}$  increases with increasing asymmetrically varying viewing geometry. However, this  
 679 behavior at first decreases with decreasing symmetrically varying geometry and then increases.  
 680 The absolute spectra in Fig. 8 shows that the large phase angles in the asymmetric viewing  
 681 geometry especially 13°-40° (Fig. 8; red) and 13°-50° (Fig. 8; violet) shows a broad absorption  
 682 band extending from 22 to 100  $\mu\text{m}$ .

683

### 684 **5.1.3 Dependency of 3D surface roughness**

685 Throughout the study, it is evident that all internal Mukundpura surfaces (B-E) for all  
 686 spectral regions from UV-FIR preserve their characteristic band absorption centers irrespective  
 687 of the differences in the viewing angle and the surface roughness for the corresponding spectral  
 688 region such as

- 689 a) Fresnel peak for carbon in UV region (Fig. 4), 0.7  $\mu\text{m}$  feature weak or null indicating  
 690 the presence of Fe-poor phyllosilicates in the VIS-IR region (Fig. 5),
- 691 b) fundamental OH- absorption featured centered at 2.72  $\mu\text{m}$  indicating the presence of  
 692 Mg-serpentine in the NIR spectral region (Fig. 6),
- 693 c) fundamental stretching and bending modes of SiO<sub>4</sub> near 9  $\mu\text{m}$  and 22  $\mu\text{m}$  respectively  
 694 along with the reflectance peak near 16  $\mu\text{m}$  indicating Mg-OH librations in  
 695 phyllosilicates which further confirming the presence of volumetrically abundant Mg-  
 696 rich phyllosilicates such as Mg-serpentine within Mukundpura bulk mineralogy in  
 697 the mid-far IR spectral region (MIR in Fig. 7 and FIR in Fig. 8).

698 Overall, it can be confidently stated that Mukundpura sample obtained has homogeneous  
 699 bulk mineralogy for all the intrinsic surfaces.

700 Varying viewing geometry either symmetrically and asymmetrically exhibit characteristic  
 701 trends in the spectral parameters such as spectral slopes (VIS-IR in Fig. 5) and absorption band  
 702 depths (NIR in Fig. 6 and MIR in Fig. 7) for the corresponding spectral region depending on the  
 703 mineralogical indicator (See Section 5.1.2) for each of the respective surface.

704 Yet, each internal surface of Mukundpura differs in the nature of their absolute spectral  
 705 shape and overall reflectance value variations for a fixed viewing angle throughout the spectral  
 706 range (UV-FIR). This difference is attributed to the 3D roughness of the surface itself and its  
 707 variation for different surfaces (Fig. 1b-h). The resulting spectral shape for a fixed viewing angle  
 708 for all intrinsic surfaces (B-E) is influenced by their respective roughness which defines the  
 709 number and area of different reflecting/sloping faces and their corresponding reflecting angles  
 710 with respect to the direction of the incident light.

711 This compels us to be careful while performing spectral parameter analysis of the  
 712 remotely sensed data of rough and rocky surface target such as Ryugu and Bennu which has  
 713 boulder-filled rough terrains with basically no smooth regions.

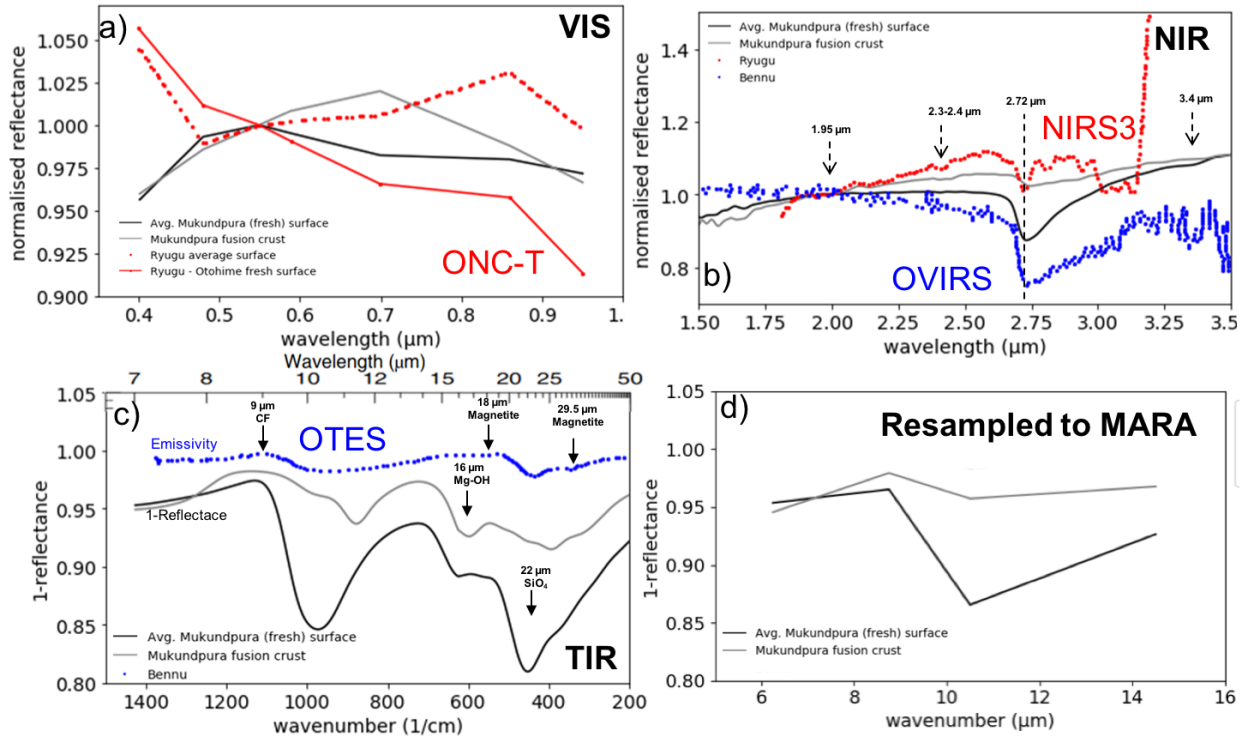
714

715

716

## 717 5.2. Application to Hayabusa 2 & OSIRIS-REx

718 For comparison, Mukundpura's fusion crust (surface A) spectra (Fig. 10; gray) and the  
 719 average surface (average of surfaces B-E) spectra (Fig. 10; black) for viewing geometry 13°-20°  
 720 is chosen to compare with the remotely sensed spectra of Ryugu (Fig. 10; red) and Bennu (Fig.  
 721 10; blue) for the respective spectral region, VIS-IR (Fig. 10a), NIR (Fig. 10b), and thermal-  
 722 infrared (TIR; Fig. 10c,d). The spectra of Ryugu and Bennu for its respective spectral range  
 723 shown in Fig. 10 are obtained by extracting the published spectral data by *Kitazato et al.* [2019],  
 724 *Tatsumi et al.* [2019] and *Hamilton et al.* [2019] respectively using an online tool,  
 725 WebPlotDigitizer (<https://automeris.io/WebPlotDigitizer/>).



726  
727

728 **Figure 10.** Comparison of Mukundpura fusion crust and average intrinsic surface spectra  
 729 compared with the extracted Ryugu and Bennu spectra [*Kitazato et al.*, 2019; *Tatsumi et al.*,  
 730 2019] and [*Hamilton et al.*, 2019] respectively using an online tool, WebPlotDigitizer  
 731 (<https://automeris.io/WebPlotDigitizer/>). a) VIS-IR region; Mukundpura vs ONC-T data of  
 732 Ryugu for its average surface and fresh Otohime surface, b) NIR region spectra of Mukundpura,  
 733 Bennu (from OVIRS), and Ryugu (NIRS3), and c) MIR region; Mukundpura vs Bennu from  
 734 OTES, d) Mukundpura fusion crust and average intrinsic surface spectra resampled to MARA-  
 735 TIR bands.

736

### 737 5.2.1 Hayabusa2/ONC-T in 0.4-1 μm

738 ONC-T data shows that Ryugu's surface is covered by numerous boulders (number  
 739 density twice as that of Itokawa) of scale-invariant varying brightness; where brighter boulders  
 740 are associated with smooth and layered surface and the darker boulders are associated with  
 741 rugged and crumbling rough surface [*Sasaki et al.*, 2019]. These differences in brightness is  
 742 contributed mainly by degrees of space weathering but less contributed by compositional  
 743 variations [*Sasaki et al.*, 2019].

744 The spectral characterization of various boulders across Ryugu surface using ONC-T data  
745 by [Tatsumi *et al.*, 2019] shows that fresh surfaces show blue spectra and while exposed to space  
746 weathering processes, the spectra reddens. This conclusion is supported by studying the spectral  
747 nature of two faces of the largest boulder Otohime Saxum (~140 m), one which is moderately  
748 sloped face whose spectra is comparable to the average Ryugu spectra (Fig. 10a; red-dotted line)  
749 and the other is cliff-like face which could have formed by recent impacts or landslides shows  
750 bluer spectra (Fig. 10a; solid-red) [Tatsumi *et al.*, 2019]. The Ryugu spectra, both average and  
751 Otohime spectra, plotted in Fig. 10a is extracted from [Tatsumi *et al.*, 2019].

752 Tatsumi *et al.* (2019) also studied the spectral parameters such as spectral slope v-to-p  
753 slope ( $\text{Ref}_{0.55}/\text{R}_{0.95}$ ) and ul-to-v slope ( $\text{Ref}_{0.40}/\text{Ref}_{0.55}$ ). All Ryugu spectra have ul-band upturn,  
754 0.40  $\mu\text{m}$  upturn, (Fig. 10a; red-dotted line) and this value vary among boulders of varying sizes  
755 and relates to atleast two different processes on Ryugu's surface; one which affects the spectral  
756 slopes could be related to space weathering [Ivanova *et al.*, 2010; Lantz *et al.*, 2017; Nakamura,  
757 2005] and the other which affects the ul-band upturn could correspond to degree of aqueous  
758 alteration [Hiroi *et al.*, 1996] and/or the presence of carbon contents [Hendrix *et al.*, 2016].  
759 However, Mukundpura spectra for both fusion crust (Fig. 10a; gray) and the interior surfaces  
760 (Fig. 10a; black) have ul-band downturn. The average surface spectra in Fig. 10a for  
761 Mukundpura represents the mineralogy of interior which is devoid of any space weathering such  
762 as solar wind irradiation and micro-meteorite impacts and solar radiation heating processes.  
763 Though fusion crust is thermally altered, it is still devoid of signatures of prolonged space  
764 weathering processes as they are lost during the atmospheric entry. This may suggest that ul-  
765 upturn of Ryugu spectra may represent the space weathering processes; however, the differences  
766 in degree of aqueous alteration and presence of carbon content from Mukundpura should be  
767 considered.

768 The average intrinsic Mukundpura VIS-IR spectra (Fig. 10a; black) after 0.55  $\mu\text{m}$   
769 behaves similar to the fresh Otohime surface with the blue-sloped (negative-sloped) spectra with  
770 minor absorption band around 0.7  $\mu\text{m}$  and absorption band after 0.88  $\mu\text{m}$ ; however, the degree of  
771 slope for fresher Ryugu spectra is slightly bluer than that of fresh Mukundpura surface.

772 Overall, the fusion crust spectra of Mukundpura spectra as a concave-shape with the  
773 reflectance maximum at 0.7  $\mu\text{m}$  which confirms the loss of water due to atmospheric heating and  
774 the absorption feature after 0.7  $\mu\text{m}$  may further indicate the presence of anhydrous minerals  
775 which is dehydrated from their hydrous counterparts. It is also important to note the reddening of  
776 the fusion crust spectra relative to the intrinsic Mukundpura surfaces up to 0.7  $\mu\text{m}$ . The slope of  
777 the fusion crust and Ryugu spectra in 0.55-0.7  $\mu\text{m}$  is comparable. Thus, the reddening of the  
778 Ryugu spectra in relative to the fresh Otohime surface could be explained by solar radiative  
779 heating in its past.

780

### 781 **5.2.2 Hayabusa2/NIRS3 and OSIRIS-REX/OVIRS in 1.5-3.5 $\mu\text{m}$**

782 *Kitazato et al.* [2019] study shows that the thermally and radiometrically calibrated  
783 spectral data from NIRS3/Hayabusa2 reveals that near-infrared (NIR) reflectance spectra of  
784 entire Ryugu exhibit a spectrally 'red' (positive) continuum slope spectra with a weak, narrow  
785 absorption feature centered at 2.72  $\mu\text{m}$  indicating the presence of OH-bearing minerals, most  
786 likely Mg-rich phyllosilicates throughout the surface. The study [Kitazato *et al.*, 2019] also  
787 suggests that intensity of 2.72  $\mu\text{m}$  band has positive correlation with estimated surface  
788 temperature but when normalized for observed temperature, the intensity of 2.72  $\mu\text{m}$  shows no  
789 correlation with topographic/morphologic features. The absorption strength of this band for the

790 normalized NIRS3 spectra ranges from 7-10%. This weak OH absorption feature and dark  
791 surface of Ryugu is attributed to either or all of the following conditions; early geologic history  
792 where inherent chemical composition with low water/rock ratio, and ongoing processes such as  
793 solar radiative heating during close approach to Sun and continuous space weathering processes  
794 such as solar-wind irradiation and micrometeorite impacts [Kitazato *et al.*, 2019]. The proposed  
795 possible compositional analogues of Ryugu are CMs and CIs [Le Corre *et al.*, 2017; Moskovitz *et*  
796 *al.*, 2013; Perna *et al.*, 2017; Vilas, 2008].

797 On the other hand, OVIRS/OSIRIS-REx spectral data of Bennu analyzed by Hamilton *et*  
798 *al.* [2019] exhibits spectrally “blue” (negative) continuum slope comparable to telescope data by  
799 Clark *et al.* [2011] along with the stronger 2.7  $\mu\text{m}$  OH-absorption feature centered around  $2.74 \pm$   
800  $0.01 \mu\text{m}$  for all OVIRS spectra and corresponds to meteorites having petrologic types of CM2.1-  
801 2.2 those have absorption band centers at 2.72  $\mu\text{m}$  [Takir *et al.*, 2013]. Hamilton *et al.* [2019]  
802 stresses that though negative or blue spectral slope of carbonaceous materials could be attributed  
803 to space weathering [Brunetto *et al.*, 2014; Lantz *et al.*, 2018; Thompson *et al.*, 2019], there is no  
804 sufficient information to confidently attribute the spectral slope of Bennu to space weathering or  
805 the presence of fine-particulate magnetite and/or insoluble inorganic material, however, the  
806 detailed analysis of high spatial resolution OVIRS data will further help us to draw conclusions.

807 In order to compare the NIR spectra of Ryugu and Bennu with our studied CM-type  
808 Mukundpura rock, we first extracted spectra of NIRS3/Ryugu from Fig. 1B of Kitazato *et al.*  
809 (2019) and OVIRS/Bennu spectra from Fig.1 of Hamilton *et al.* (2019). We then normalized the  
810 NIR spectra of Ryugu (Fig. 10b; red), Bennu (Fig. 10b; blue), the fusion crust (surface A) and  
811 average surface spectra (average spectra of surfaces B,C,D,E) of Mukundpura for viewing  
812 geometry 13°-20° as it closely corresponds to nadir viewing of NIRS3 (Fig. 10b; gray and blue  
813 respectively) to a reflectance value of 1.0 at 2  $\mu\text{m}$  as shown in Fig. 10b.

814 *NIR spectral slope:* For the spectral region 1.5-2.7  $\mu\text{m}$ , the slope of the normalized NIR  
815 spectra (Fig. 10b) of average Mukundpura surface spectra (Fig. 10b; black) is nearly flat and  
816 unlike red-sloped Ryugu spectra (Fig. 10b; red) and blue-sloped Bennu spectra (Fig. 10b; blue).  
817 However, the fusion crust spectra (Fig. 10b; gray) have slightly redder slope compared to the  
818 fresh Mukundpura surface (Fig. 10b; black). This suggests that the reddening of the NIR  
819 continuum spectra of Mukundpura is caused by the thermal weathering of fusion crust during the  
820 path of meteorite fall. The redder slope of Ryugu spectra (Fig. 10b; red) could therefore be  
821 associated to heating of Ryugu either by solar radiative heating during shortened perihelion  
822 distances in its past [Kitazato *et al.*, 2019].

823 *NIR absorption bands:* Fig. 10b shows that Bennu’s OVIRS spectrum (Fig. 10b; blue)  
824 has the strongest and broad asymmetric 2.7  $\mu\text{m}$  absorption band compared to Mukundpura and  
825 Ryugu NIR spectra. The average surface spectrum of Mukundpura (Fig. 10b; black) has  
826 comparatively weaker absorption feature centered at 2.72  $\mu\text{m}$  with an asymmetric spectral shape.  
827 However, NIR spectrum of fusion crust of Mukundpura has the highly subdued, broader  
828 asymmetric OH-absorption feature with its center slightly moved longward from its average  
829 surface spectrum, centered at 2.74  $\mu\text{m}$  similar to Bennu spectrum. On the other hand, Ryugu  
830 spectrum shows the weak but sharp symmetric OH-absorption feature centered at 2.72  $\mu\text{m}$ .  
831 Nevertheless, in the shorter wavelengths (1.75-2.5  $\mu\text{m}$ ), both fusion crust of Mukundpura (Fig.  
832 10b; gray) and Ryugu (Fig. 10b; red) share significantly similar spectral shape with spectral  
833 features such as; a) a minor absorption band in 2.3-2.4  $\mu\text{m}$  region which is characteristic spectral  
834 feature of metal-OH bond in serpentines [Cloutis *et al.*, 2011], and the minor broad absorption  
835 bands near 1.95  $\mu\text{m}$  with spectral shoulders near 1.9  $\mu\text{m}$  and 2.08  $\mu\text{m}$  (Fig.9b); and these features

836 are not prominent in the fresh average surface spectra of Mukundpura. *Kitazato et al.* [2019]  
837 mentioned that no existing meteorite samples reflectance spectra matches with Ryugu visible to  
838 NIR wavelength. Our results reveal the intrinsic (B-E) surface of Mukundpura shows  
839 fundamental absorption as 2.72  $\mu\text{m}$  with an additional shared band absorption near 1.95  $\mu\text{m}$  and  
840 2.3-2.4  $\mu\text{m}$ . Even the fusion crust hosts considerable absorption at this wavelength. Thus,  
841 thermally metamorphosed and shocked Mukundpura with diagnostic 2.72  $\mu\text{m}$  absorption is  
842 highly comparable to the Ryugu. Therefore, supporting that Ryugu surface has experienced  
843 extensive heating in its geologic past.

844 Overall reddening of spectral shape of fusion crust with similar spectral shape near 1.95,  
845 2.3-2.4  $\mu\text{m}$ , and weak 2.7  $\mu\text{m}$  band as Ryugu could explain the heating of Ryugu surface in its  
846 history. However, the strong asymmetric 2.72  $\mu\text{m}$  band of Mukundpura internal surface  
847 resembling Bennu spectrum suggests that Bennu has not undergone significant heating compared  
848 to Ryugu. In addition to this, the 3.4  $\mu\text{m}$  absorption band corresponding to presence of organics  
849 suggested for Bennu [*Lauretta et al.*, 2019] can be traced in the average surface spectra of  
850 Mukundpura in Fig. 10b which is much evident in the continuum removed spectra in Fig. 6iii  
851 suggesting the presence of organics in the fresh Mukundpura surface, however, this feature is  
852 much subdued in the fusion crust spectra (Fig. 10b).

853

### 854 **5.2.3 OSIRIS-REX/OTES in 7-50 $\mu\text{m}$**

855 OTES spectrometer onboard OSIRIS-Rex maps the emissivity spectrum of Bennu at the  
856 spectral range 7-50  $\mu\text{m}$ . *Hamilton et al.* [2019] shows that calibrated average disk integrated  
857 spectrum of Bennu exhibits the CF position similar to that of the CM1/2 and CM2 petrologic  
858 types which is the emissivity maximum around 9  $\mu\text{m}$  indicating the presence of stretching modes  
859 of  $\text{SiO}_4$  in the hydrous silicates. To compare Mukundpura spectra with Bennu's OTES/OSIRIS-  
860 REX spectra, we first extracted the calibrated disk-integrated average emissivity spectrum of  
861 Bennu from Fig. 3 of *Hamilton et al.* [2019]. Bennu spectrum also exhibits the absorption feature  
862 near 22  $\mu\text{m}$  indicative of the presence of corresponding bending modes of  $\text{SiO}_4$  in the hydrous  
863 silicates. In addition to that, OTES spectrum of Bennu spectrum also exhibits the spectral  
864 indicators of presence of magnetite which includes the minor absorption bands near 18  $\mu\text{m}$  and  
865 29.5  $\mu\text{m}$ . OTES data analyzed by *Hamilton et al.* [2019] also shows that entire Bennu surface is  
866 spatially uniform at 80 m spatial scale with similar range of particle sizes for each pixel at large  
867 spatial scales.

868 In order to compare the emissivity spectrum of Bennu with the measured reflectance of  
869 Mukundpura surface and fusion crust (Fig. 10c), we estimated 1-reflectance of Mukundpura  
870 spectra as a proxy for emissivity (Kirchoff's law). Bennu's OTES spectrum (Fig. 10c; blue)  
871 resembles the average Mukundpura surface (Fig. 10c; black) except for the lack of characteristic  
872 Mg-OH band near 16  $\mu\text{m}$  which is the indicator of Mg-serpentine of Mukundpura. As suggested  
873 by *Hamilton et al.* [2019], the lack of this 16  $\mu\text{m}$  feature could be attributed to presence of non-  
874 Mg endmember (possibly Fe-bearing phyllosilicates), modest heating, disorder and/or particle  
875 sizes. However, thermally altered Mukundpura which has indicators of loss of water in the VIS-  
876 NIR spectral region, still preserves the 16  $\mu\text{m}$  Mg-OH absorption band (Fig. 10c).

877 Our spectral analysis revealed that both Bennu and Mukundpura surface has CF band  
878 near 9  $\mu\text{m}$  and the absorption band near 22  $\mu\text{m}$  suggestive of the hydrous minerals. This suggests  
879 that Bennu surface is volumetrically dominated by the phyllosilicates and therefore indicating the  
880 aqueous alteration of the parent body. However, OTES spectrum of Bennu possess lesser  
881 spectral contrast compared to average Mukundpura spectrum (Fig. 10c; black) especially in the

882 regions of silicate stretching bands (9-14.5  $\mu\text{m}$ ) where Benu spectrum exhibits a broader, bowl-  
883 like shape unlike the sharp distinct transparency features resulting from volume scattering in the  
884 case of average Mukundpura surface. This may indicate that Benu's surface is dominated by  
885 amorphous/disordered component [Hamilton *et al.*, 2019] unlike ordered/crystalline Mukundpura  
886 interior surface and attribution of this amorphous/disordered behavior to the lack of 16  $\mu\text{m}$   
887 should be studied further. 18  $\mu\text{m}$  absorption feature corresponding to magnetite can be traced for  
888 a weak absorption for Mukundpura for its average fresh surface.

889 The 1-reflectance TIR spectra of fusion crust (Fig. 10c; gray) exhibits sharp-fine 12  $\mu\text{m}$   
890 feature with minor absorption bands around 10.6  $\mu\text{m}$ , 11.4  $\mu\text{m}$ , and 12.4  $\mu\text{m}$  indicative of the  
891 back-transformation of hydrous minerals to their corresponding anhydrous silicates, olivine and  
892 pyroxene [Beck *et al.*, 2018]. The overall shape of fusion crust in TIR spectral region is different  
893 from that of Benu's spectrum which further confirms that Benu's surface is dominated by the  
894 aqueously altered minerals.

895

### 896 **5.2.3 Hayabusa2/MASCOT/MARA in 5-16 $\mu\text{m}$**

897 Hayabusa2 also carried two surface spectrometers with the DLR's MASCOT lander; 6-  
898 band thermal radiator (MARA) and a hyperspectral infrared microscope (MicrOmega). MARA  
899 houses 4 bandpass spectral channels in the range of 5.5–7  $\mu\text{m}$ , 8–9.5  $\mu\text{m}$ , 9.5–11.5  $\mu\text{m}$ , and 13.5–  
900 15.5  $\mu\text{m}$ , as well as one long-pass channel sensitive in the  $>3$   $\mu\text{m}$  range [Grott *et al.*, 2017]. In  
901 Fig. 10d, the average fresh surface and fusion crust of Mukundpura and Benu OTES spectra is  
902 resampled to MARA spectral bands. This will further help MARA data analysis to be compared  
903 with Mukundpura as a Ryugu's analogue.

904

## 905 **6 Conclusions**

906 In this work, the ultraviolet to far-infrared reflectance spectra of extremely fresh  
907 carbonaceous chondrite rock (Mukundpura meteorite) have been studied for symmetrically and  
908 asymmetrically varying viewing geometries. The comparison of the spectral behavior of the  
909 fusion crust to the fresh interiors further helps to understand the evolution of the spectral  
910 behavior due to thermal alteration during atmospheric entry. The systematic spectral behavior  
911 trend in the reflectance of CM chondrites (Mukundpura with intrinsic and fusion crust) in Fresnel  
912 peak in UV, visible-IR slope after 0.55  $\mu\text{m}$ , fundamental hydroxyl (OH<sup>-</sup>) band strength in NIR  
913 and the Christiansen Feature minimum at MIR with symmetric and asymmetric varying  
914 geometry is observed for the first time. The change in overall reflectance value and the spectral  
915 shape due to changes in 3D surface roughness is observed in the study. In addition to  
916 photometric corrections which corrects for viewing geometry, the significant spectral effects due  
917 to the varying 3D roughness of the rocky boulder-like terrain of Ryugu and Benu should be  
918 carefully considered while attempting to quantify the mineralogy interpretations such as amount  
919 of water, magnetite, carbon, hydrous minerals etc for their corresponding spectral regions. The  
920 phase angle/viewing geometry dependent UV-FIR reflectance spectroscopy of fresh CM rock  
921 reveals that the fundamental absorption band centers at all wavelengths are not (or least) affected  
922 by surface roughness and viewing geometry; however, their band strengths and spectral band  
923 shape varies.

924 The results reveal that the thermally metamorphosed and shocked Mukundpura fusion  
925 crust with diagnostic 2.72  $\mu\text{m}$  absorption is comparable to the Ryugu. Therefore, supporting that  
926 Ryugu surface has experienced extensive heating in its geologic past. The asymmetric 3  $\mu\text{m}$  band  
927 of Benu is significantly comparable to the strong asymmetric absorption band of intrinsic

928 Mukundpura surfaces, which further supports that Bennu's upper layer had not undergone  
929 heating compared to Ryugu surface. Instead of powdered samples of meteorites, the direct  
930 spectral investigation of varying surface roughness of single Mukundpura sample under varying  
931 viewing geometry therefore potentially support the spectral analysis of Ryugu and Bennu  
932 spectral data from orbit and surface and future exploration of C-type asteroids.

933

### 934 **Acknowledgements**

935 The authors thank DLR/DAAD Doctorate Fellowship to Indhu Varatharajan for funding  
936 her PhD work at PSL-DLR. A portion of this research was supported by the European Union's  
937 Horizon 2020 research and innovation program. Europlanet 2020 RI has received funding from  
938 the European Union's Horizon 2020 research and innovation programme under grant agreement  
939 No 654208. The work at PRL is supported by Department of Space, Government of India.  
940

### 941 **References**

942 Anders, E., and N. Grevesse (1989), Abundances of the elements: Meteoritic and solar,  
943 *Geochimica et Cosmochimica Acta*, 53(1), 197-214, doi:[https://doi.org/10.1016/0016-](https://doi.org/10.1016/0016-7037(89)90286-X)  
944 [7037\(89\)90286-X](https://doi.org/10.1016/0016-7037(89)90286-X).

945 Applin, D. M., M. R. M. Izawa, E. A. Cloutis, J. J. Gillis-Davis, K. M. Pitman, T. L. Roush, A.  
946 R. Hendrix, and P. G. Lucey (2018), Ultraviolet spectral reflectance of carbonaceous materials,  
947 *Icarus*, 307, 40-82, doi:<https://doi.org/10.1016/j.icarus.2018.02.012>.

948 Baliyan, S., and D. Ray (2019), Colour Cathodoluminescence study of forsteritic Olivine in  
949 Mukundpura (CM2) meteorite, 50th Lunar and Planetary Science Conference, Abstract #1603.

950 Barber, D. J. (1981), Phyllosilicates and other layer-structured minerals in stony meteorites, *Clay*  
951 *Miner.*, 20, 415–454.

952 Barrat, J. A., B. Zanda, F. Moynier, C. Bollinger, C. Liorzou, and G. Bayon (2012),  
953 Geochemistry of CI chondrites: Major and trace elements, and Cu and Zn Isotopes, *Geochimica*  
954 *et Cosmochimica Acta*, 83, 79-92, doi:<https://doi.org/10.1016/j.gca.2011.12.011>.

955 Beck, P., A. Garenne, E. Quirico, L. Bonal, G. Montes-Hernandez, F. Moynier, and B. Schmitt  
956 (2014), Transmission infrared spectra (2–25 $\mu\text{m}$ ) of carbonaceous chondrites (CI, CM, CV–CK,  
957 CR, C2 ungrouped): Mineralogy, water, and asteroidal processes, *Icarus*, 229, 263-277,  
958 doi:<https://doi.org/10.1016/j.icarus.2013.10.019>.

959 Beck, P., A. Maturilli, A. Garenne, P. Vernazza, J. Helbert, E. Quirico, and B. Schmitt (2018),  
960 What is controlling the reflectance spectra (0.35–150  $\mu\text{m}$ ) of hydrated (and dehydrated)  
961 carbonaceous chondrites?, *Icarus*, 313, 124-138, doi:<https://doi.org/10.1016/j.icarus.2018.05.010>.

962 Beck, P., et al. (2010), Hydrous mineralogy of CM and CI chondrites from infrared spectroscopy  
963 and their relationship with low albedo asteroids, *Geochimica et Cosmochimica Acta*, 74(16),  
964 4881-4892, doi:<https://doi.org/10.1016/j.gca.2010.05.020>.

- 965 Browning, L. B., H. Y. McSween, and M. E. Zolensky (1996), Correlated alteration effects in  
966 CM carbonaceous chondrites, *Geochimica et Cosmochimica Acta*, 60(14), 2621-2633,  
967 doi:[https://doi.org/10.1016/0016-7037\(96\)00121-4](https://doi.org/10.1016/0016-7037(96)00121-4).
- 968 Brunetto, R., et al. (2014), Ion irradiation of Allende meteorite probed by visible, IR, and Raman  
969 spectroscopies, *Icarus*, 237, 278-292, doi:<https://doi.org/10.1016/j.icarus.2014.04.047>.
- 970 Christensen, P. R., et al. (2018), The OSIRIS-REx Thermal Emission Spectrometer (OTES)  
971 Instrument, *Space Science Reviews*, 214(5), 87, doi:10.1007/s11214-018-0513-6.
- 972 Clark, B. E., et al. (2011), Asteroid (101955) 1999 RQ36: Spectroscopy from 0.4 to 2.4 $\mu$ m and  
973 meteorite analogs, *Icarus*, 216(2), 462-475, doi:<https://doi.org/10.1016/j.icarus.2011.08.021>.
- 974 Clark, R. N., T. V. V. King, and N. S. Gorelick (1987), Automatic continuum analysis of  
975 reflectance spectra., In: *Proceedings, Third AIS Workshop, 2–4 June, 1987, JPL Publication*, 97-  
976 130, 138–142.
- 977 Clark, R. N., and T. L. Roush (1984), Reflectance spectroscopy: Quantitative analysis techniques  
978 for remote sensing applications, *Journal of Geophysical Research: Solid Earth*, 89(B7), 6329-  
979 6340, doi:10.1029/JB089iB07p06329.
- 980 Cloutis, E. A., P. Hudon, T. Hiroi, M. J. Gaffey, and P. Mann (2011), Spectral reflectance  
981 properties of carbonaceous chondrites: 2. CM chondrites, *Icarus*, 216(1), 309-346,  
982 doi:<https://doi.org/10.1016/j.icarus.2011.09.009>.
- 983 DellaGiustina, D. N., et al. (2019), Properties of rubble-pile asteroid (101955) Bennu from  
984 OSIRIS-REx imaging and thermal analysis, *Nature Astronomy*, 3(4), 341-351,  
985 doi:10.1038/s41550-019-0731-1.
- 986 Farmer, V. C. (1974), *The Infrared Spectra of Minerals*, Mineralogical Society, London,  
987 Monograph 4(331), doi:<http://dx.doi.org/10.1180/mono-4.15>.
- 988 Flynn, G. J., G. J. Consolmagno, P. Brown, and R. J. Macke (2018), Physical properties of the  
989 stone meteorites: Implications for the properties of their parent bodies, *Geochemistry*, 78(3),  
990 269-298, doi:<https://doi.org/10.1016/j.chemer.2017.04.002>.
- 991 Garenne, A., P. Beck, G. Montes-Hernandez, O. Brissaud, B. Schmitt, E. Quirico, L. Bonal, C.  
992 Beck, and K. T. Howard (2016), Bidirectional reflectance spectroscopy of carbonaceous  
993 chondrites: Implications for water quantification and primary composition, *Icarus*, 264, 172-183,  
994 doi:<https://doi.org/10.1016/j.icarus.2015.09.005>.
- 995 Garenne, A., P. Beck, G. Montes-Hernandez, R. Chiriach, F. Toche, E. Quirico, L. Bonal, and B.  
996 Schmitt (2014), The abundance and stability of “water” in type 1 and 2 carbonaceous chondrites  
997 (CI, CM and CR), *Geochimica et Cosmochimica Acta*, 137, 93-112,  
998 doi:<https://doi.org/10.1016/j.gca.2014.03.034>.

- 999 Glotch, T. D., G. R. Rossman, and O. Aharonson (2007), Mid-infrared (5–100  $\mu\text{m}$ ) reflectance  
1000 spectra and optical constants of ten phyllosilicate minerals, *Icarus*, 192(2), 605-622,  
1001 doi:<https://doi.org/10.1016/j.icarus.2007.07.002>.
- 1002 Grott, M., J. Knollenberg, B. Borgs, F. Hänschke, E. Kessler, J. Helbert, A. Maturilli, and N.  
1003 Müller (2017), The MASCOT Radiometer MARA for the Hayabusa 2 Mission, *Space Science*  
1004 *Reviews*, 208(1), 413-431, doi:10.1007/s11214-016-0272-1.
- 1005 GSI (2017), Preliminary Study Note on the Meteorite Fall at Mukundpura, Bhankrota, Jaipur,  
1006 Official report from Geological Survey of India, Govt of India, Link:  
1007 <https://employee.gsi.gov.in/cs/groups/public/documents/document/b3zp/mtq4/~edisp/dcport1gsi>  
1008 [govi148390.pdf](https://employee.gsi.gov.in/cs/groups/public/documents/document/b3zp/mtq4/~edisp/dcport1gsi_govi148390.pdf).
- 1009 Haberle, C. W., P. R. Christensen, L. A. J. Garvie, V. E. Hamilton, R. D. Hanna, H. C. C. Jr., D.  
1010 S. Laurreta, and a. t. O.-R. Team. (2019), The Mineralogy of Recently Fallen Carbonaceous  
1011 Meteorites, Mukundpura and Sutter's Mill, in the Context of Asteroid (101955) Bennu, 50th  
1012 Lunar and Planetary Science Conference, Abstract #2144.
- 1013 Hamilton, V. E., et al. (2019), Evidence for widespread hydrated minerals on asteroid (101955)  
1014 Bennu, *Nature Astronomy*, 3(4), 332-340, doi:10.1038/s41550-019-0722-2.
- 1015 Hanowski, N. P., and A. J. Brearley (2001), Aqueous alteration of chondrules in the CM  
1016 carbonaceous chondrites, Allan Hills 81002. , *Geochim. Cosmochim. Acta* 65, 495–518.
- 1017 Hendrix, A. R., F. Vilas, and J.-Y. Li (2016), The UV signature of carbon in the solar system,  
1018 *Meteoritics & Planetary Science*, 51(1), 105-115, doi:doi:10.1111/maps.12575.
- 1019 Hiroi, T., M. E. Zolensky, C. M. Pieters, and M. E. Lipschutz (1996), Thermal metamorphism of  
1020 the C, G, B, and F asteroids seen from the 0.7  $\mu\text{m}$ , 3  $\mu\text{m}$ , and UV absorption strengths in  
1021 comparison with carbonaceous chondrites, *Meteoritics & Planetary Science*, 31(3), 321-327,  
1022 doi:doi:10.1111/j.1945-5100.1996.tb02068.x.
- 1023 Howard, K. T., G. K. Benedix, P. A. Bland, and G. Cressey (2009), Modal mineralogy of CM2  
1024 chondrites by X-ray diffraction (PSD-XRD). Part 1: Total phyllosilicate abundance and the  
1025 degree of aqueous alteration, *Geochimica et Cosmochimica Acta*, 73(15), 4576-4589,  
1026 doi:<https://doi.org/10.1016/j.gca.2009.04.038>.
- 1027 Howard, K. T., G. K. Benedix, P. A. Bland, and G. Cressey (2011), Modal mineralogy of CM  
1028 chondrites by X-ray diffraction (PSD-XRD): Part 2. Degree, nature and settings of aqueous  
1029 alteration, *Geochimica et Cosmochimica Acta*, 75(10), 2735-2751,  
1030 doi:<https://doi.org/10.1016/j.gca.2011.02.021>.
- 1031 Ivanova, M. A., C. A. Lorenz, M. A. Nazarov, F. Brandstaetter, I. A. Franchi, L. V. Moroz, R. N.  
1032 Clayton, and A. Y. Bychkov (2010), Dhofar 225 and Dhofar 735: Relationship to CM2  
1033 chondrites and metamorphosed carbonaceous chondrites, Belgica-7904 and Yamato-86720,  
1034 *Meteoritics & Planetary Science*, 45(7), 1108-1123, doi:doi:10.1111/j.1945-5100.2010.01064.x.

- 1035 Izawa, M. R. M., V. Reddy, L. L. Corre, A. McGraw, J. A. Sanchez, E. A. Cloutis, K.  
1036 Yamashita, A. P. Jephcoat, D. M. Applin, and B. J. Hall (2019), Discovery of a Possible CM2  
1037 Carbonaceous Chondrite Parent Body in the Near-earth Asteroid Population. , 50th Lunar and  
1038 Planetary Science Conference, Abstract #3174.
- 1039 Jacinto, A.-A., et al. (2013), UV to far-IR reflectance spectra of carbonaceous chondrites – I.  
1040 Implications for remote characterization of dark primitive asteroids targeted by sample-return  
1041 missions, *Monthly Notices of the Royal Astronomical Society*, 437(1), 227-240,  
1042 doi:10.1093/mnras/stt1873.
- 1043 Kitazato, K., et al. (2019), The surface composition of asteroid 162173 Ryugu from Hayabusa2  
1044 near-infrared spectroscopy, *Science*, eaav7432, doi:10.1126/science.aav7432.
- 1045 Lantz, C., R. P. Binzel, and F. E. DeMeo (2018), Space weathering trends on carbonaceous  
1046 asteroids: A possible explanation for Bennu's blue slope?, *Icarus*, 302, 10-17,  
1047 doi:https://doi.org/10.1016/j.icarus.2017.11.010.
- 1048 Lantz, C., R. Brunetto, M. A. Barucci, S. Fornasier, D. Baklouti, J. Bourçois, and M. Godard  
1049 (2017), Ion irradiation of carbonaceous chondrites: A new view of space weathering on primitive  
1050 asteroids, *Icarus*, 285, 43-57, doi:https://doi.org/10.1016/j.icarus.2016.12.019.
- 1051 Lauretta, D. S., et al. (2019), The unexpected surface of asteroid (101955) Bennu, *Nature*,  
1052 568(7750), 55-60, doi:10.1038/s41586-019-1033-6.
- 1053 Lauretta, D. S., X. Hua, and P. R. Buseck (2000), Mineralogy of fine-grained rims in the  
1054 ALH81002 CM chondrite. , *Geochim. Cosmochim. Acta* 64, 3263–3273.
- 1055 Le Corre, L., V. Reddy, J. A. Sanchez, D. Takir, E. Cloutis, A. Thirouin, K. J. Becker, J.-Y. Li,  
1056 S. Sugita, and E. Tatsumi (2017), Ground-based characterization of Hayabusa2 mission target  
1057 asteroid 162173 Ryugu: constraining mineralogical composition in preparation for spacecraft  
1058 operations, *Monthly Notices of the Royal Astronomical Society*, 475(1), 614-623,  
1059 doi:10.1093/mnras/stx3236.
- 1060 MacKinnon, I. D. R. (1982), Ordered mixed-layer structures in the Mighei carbonaceous  
1061 chondritic matrix. , *Geochim. Cosmochim. Acta.*, 46, 479–489.
- 1062 Malavergne, V., et al. (2014), How Mercury can be the most reduced terrestrial planet and still  
1063 store iron in its mantle, *Earth and Planetary Science Letters*, 394, 186-197,  
1064 doi:https://doi.org/10.1016/j.epsl.2014.03.028.
- 1065 Matsuoka, M., T. Nakamura, T. Hiroi, K. Kitazato, M. A. T. Iwata, K. Amano, S. Kobayashi, T.  
1066 Osawa, M. Ohtake, S. Matsuura, T. Arai, H. Senshu, M. Komatsu, A. Nakato, Y. Nakauchi, C.  
1067 Pilorget, R. Brunetto, F. Poulet, L. Riu, D. Domingue, F. Vilas, D. Takir, E. Palomba, A., R. M.  
1068 Galiano, D. Perna, A. Barucci, J-P Bibring, N. Imae, A. Yamaguchi, H. Kojima, S., and S. T.  
1069 Nakazawa, M. Yoshikawa, S. Watanabe, Y. Tsuda (2019), Infrared Spectra of Asteroid Ryugu:

- 1070 Comparison to Laboratory-Measured Carbonaceous Chondrites., 50th Lunar and Planetary  
1071 Science Conference, Abstract #1534.
- 1072 Maturilli, A., J. Helbert, M. D'Amore, I. Varatharajan, and Y. Rosas Ortiz (2018a), The  
1073 Planetary Spectroscopy Laboratory (PSL): Wide spectral range, wider sample temperature range,  
1074 in *Infrared Remote Sensing and Instrumentation XXVI*, edited, doi:10.1117/12.2319944.
- 1075 Maturilli, A., J. Helbert, S. Ferrari, B. Davidsson, and M. D'Amore (2016), Characterization of  
1076 asteroid analogues by means of emission and reflectance spectroscopy in the 1- to 100- $\mu$ m  
1077 spectral range, *Earth, Planets and Space*, 68(1), 113, doi:10.1186/s40623-016-0489-y.
- 1078 Maturilli, A., J. Helbert, J. M. St. John, J. W. Head III, W. M. Vaughan, M. D'Amore, M.  
1079 Gottschalk, and S. Ferrari (2014), Komatiites as Mercury surface analogues: Spectral  
1080 measurements at PEL, *Earth and Planetary Science Letters*, 398, 58-65,  
1081 doi:http://dx.doi.org/10.1016/j.epsl.2014.04.035.
- 1082 Maturilli, A., J. Helbert, I. Varatharajan, Y Rosas Ortiz, and M. D'Amore (2018b), The Planetary  
1083 Spectroscopy Laboratory (PSL), *Earth and Planetary Science Congress (EPSC)*, Abstract:  
1084 EPSC2018-753.
- 1085 McAdam, M. M., J. M. Sunshine, K. T. Howard, and T. M. McCoy (2015), Aqueous alteration  
1086 on asteroids: Linking the mineralogy and spectroscopy of CM and CI chondrites, *Icarus*, 245,  
1087 320-332, doi:https://doi.org/10.1016/j.icarus.2014.09.041.
- 1088 Moskovitz, N. A., et al. (2013), Rotational characterization of Hayabusa II target Asteroid  
1089 (162173) 1999 JU3, *Icarus*, 224(1), 24-31, doi:https://doi.org/10.1016/j.icarus.2013.02.009.
- 1090 Nakamura, T. (2005), Post-hydration thermal metamorphism of carbonaceous chondrites,  
1091 *Journal of Mineralogical and Petrological Sciences*, 100(6), 260-272, doi:10.2465/jmps.100.260.
- 1092 Perna, D., et al. (2017), Spectral and rotational properties of near-Earth asteroid (162173) Ryugu,  
1093 target of the Hayabusa2 sample return mission\*, *A&A*, 599, L1.
- 1094 Potin, S., P. Beck, L. Bonal, B. Schmitt, F. Moynier, E. Quirico, A. Garenne, and C. Honda  
1095 (2018), Post-Accretion History and Reflectance Spectroscopy Properties of the Mukundpura  
1096 Meteorite, 81st Annual Meeting of The Meteoritical Society 2018, LPI Contrib. No. 2067.
- 1097 Potin, S., P. Beck, B. Schmitt, and F. Moynier (2019), Some things special about NEAs:  
1098 Geometric and environmental effects on the optical signatures of hydration, *Icarus*, 333, 415-  
1099 428, doi:https://doi.org/10.1016/j.icarus.2019.06.026.
- 1100 Ray, D., and A. D. Shukla (2018), The Mukundpura meteorite, a new fall of CM chondrite,  
1101 *Planetary and Space Science*, 151, 149-154, doi:https://doi.org/10.1016/j.pss.2017.11.005.

- 1102 Reuter, D. C., et al. (2018), The OSIRIS-REx Visible and InfraRed Spectrometer (OVIRS):  
1103 Spectral Maps of the Asteroid Bennu, *Space Science Reviews*, 214(2), 54, doi:10.1007/s11214-  
1104 018-0482-9.
- 1105 Richardson, S. M. (1981), Alteration of mesostasis in chondrules and aggregates from three C2  
1106 carbonaceous chondrites, *Earth Planet. Sci. Lett.*, 52, 67-75.
- 1107 Rudraswami, N. G., A. K. Naik, R. P. Tripathi, N. Bhandari, S. G. Karapurkar, M. S. Prasad, E.  
1108 V. S. S. K. Babu, and U. V. R. Vijaya Sarathi (2018), Chemical, isotopic and amino acid  
1109 composition of Mukundpura CM2.0 (CM1) chondrite: Evidence of parent body aqueous  
1110 alteration, *Geoscience Frontiers*, doi:https://doi.org/10.1016/j.gsf.2018.02.001.
- 1111 Ryskin, Y. I. (1974), *The Vibrations of Protons in Minerals: hydroxyl, water and ammonium,*  
1112 *The Infrared Spectra of Minerals*, edited by V. C. Farmer, p. 0, Mineralogical Society of Great  
1113 Britain and Ireland, doi:10.1180/mono-4.9.
- 1114 Sasaki, S., S. Sugita, E. Tatsumi, C. H. H. Miyamoto, T. Morota, O. S. Barnouin, M.  
1115 Hirabayashi, S. Kanda, M. Kanamaru, N. Hirata, T. Hiroi, T. Nakamura, T. Noguchi, R. Honda,  
1116 T. Michikami, S. Watanabe, N. Namiki, P. Michel, S. Kameda, and H. S. T. Kouyama, M.  
1117 Yamada, H. Kikuchi, D. L. Domingue, Y. Cho, K. Yoshioka, M. Hayakawa, M. Matsuoka, R.  
1118 Noguchi, N. Sakatani, H. Sawada, Y. Yokota, M. Yoshikawa (2019), Brightness and  
1119 Morphology Variations on Surface Rocks of 162173 Ryugu: Space Weathering, Breccia  
1120 Structure, and Meridional Cracks, 50th Lunar and Planetary Science Conference, Abstract:  
1121 #1368.
- 1122 Simon, A. A., D. C. Reuter, N. Goriuss, A. Lunsford, R. G. Cosentino, G. Wind, D. S. Lauretta,  
1123 and T. O.-R. Team (2018), In-Flight Calibration and Performance of the OSIRIS-REx Visible  
1124 and IR Spectrometer (OVIRS), *Remote Sensing*, 10(9), 1486.
- 1125 Sugita, S., et al. (2019), The geomorphology, color, and thermal properties of Ryugu:  
1126 Implications for parent-body processes, *Science*, eaaw0422, doi:10.1126/science.aaw0422.
- 1127 Takir, D., J. P. Emery, H. Y. Mcsween Jr., C. A. Hibbitts, R. N. Clark, N. Pearson, and A. Wang  
1128 (2013), Nature and degree of aqueous alteration in CM and CI carbonaceous chondrites,  
1129 *Meteoritics & Planetary Science*, 48(9), 1618-1637, doi:10.1111/maps.12171.
- 1130 Tatsumi, E., S. Sugita, S. Kameda, R. Honda, T. Kouyama, Y. Yokota, N. Sakatani, T. M. C.  
1131 Honda, M. Tomokatsu, M. Yamada, H., Y. C. Suzuki, M. Matsuoka, M. Hayakawa, K.  
1132 Yoshioka, K. Ogawa, H. Sawada, F. Vilas, D., and L. L. C. Domingue, S. Sasaki, T. Nakamura,  
1133 T. Hiroi (2019), Visible Color Variation of Boulders on 162173 Ryugu, 50th Lunar and  
1134 Planetary Science Conference, Abstract: #1753.
- 1135 Thompson, M. S., M. J. Loeffler, R. V. Morris, L. P. Keller, and R. Christoffersen (2019),  
1136 Spectral and chemical effects of simulated space weathering of the Murchison CM2  
1137 carbonaceous chondrite, *Icarus*, 319, 499-511, doi:https://doi.org/10.1016/j.icarus.2018.09.022.

- 1138 Tomeoka, K., and P. R. Buseck (1985), Indicators of aqueous alteration in CM carbonaceous  
1139 chondrites: Microtextures of a layered mineral containing Fe, S, O and Ni, *Geochimica et*  
1140 *Cosmochimica Acta*, 49(10), 2149-2163, doi:[https://doi.org/10.1016/0016-7037\(85\)90073-0](https://doi.org/10.1016/0016-7037(85)90073-0).
- 1141 Vilas, F. (2008), Spectral Characteristics of Hayabusa2 Near-Earth Asteroid Targets 162173  
1142 1999 JU3 and 2001 QC34, *The Astronomical Journal*, 135(4), 1101-1105, doi:10.1088/0004-  
1143 6256/135/4/1101.
- 1144 Walsh, K. J., et al. (2019), Craters, boulders and regolith of (101955) Bennu indicative of an old  
1145 and dynamic surface, *Nature Geoscience*, 12(4), 242-246, doi:10.1038/s41561-019-0326-6.
- 1146 Watanabe, S., et al. (2019), Hayabusa2 arrives at the carbonaceous asteroid 162173 Ryugu—A  
1147 spinning top-shaped rubble pile, *Science*, eaav8032, doi:10.1126/science.aav8032.
- 1148 Zega, T. J., and P. R. Buseck (2003), Fine-grained-rim mineralogy of the Cold Bokkeveld CM  
1149 chondrite, *Geochim. Cosmochim. Acta*, 67, 1711–1721.
- 1150 Zolensky, M. E., R. Barrett, and L. Browning (1993), Mineralogy and composition of matrix and  
1151 chondrule rims in carbonaceous chondrites, *Geochim. Cosmochim. Acta.*, 57, 3123–3148.